UNCLASSIFIED

SECURITY CLASSIFICATION OF THIS PAGE (When Data Entered)

REPORT DOCUMENTATION PAGE

READ INSTRUCTIONS BEFORE COMPLETING FORM

1. REPORT NUMBER
AFGL-TR-83-0236

2. GOVT ACCESSION NO.

3. RECIPIENT'S CATALOG NUMBER

4. TITLE (and Subtitle)
ANALYTIC TECHNIQUES FOR ESTIMATING VISIBLE IMAGE TRANSMISSION PROPERTIES OF THE ATMOSPHERE

5. TYPE OF REPORT & PERIOD COVERED
Scientific - Interim
Scientific Report No. 3

6. PERFORMING ORG. REPORT NUMBER
SIO Ref. 84-6

7. AUTHOR(s)
Wayne S. Hering

8. CONTRACT OR GRANT NUMBER(s)
F19628-82-C-0060

9. PERFORMING ORGANIZATION NAME AND ADDRESS
University of California, San Diego
Visibility Laboratory
La Jolla, California 92093

10. PROGRAM ELEMENT, PROJECT, TASK AREA & WORK UNIT NUMBERS
62101F
7670-14-02

11. CONTROLLING OFFICE NAME AND ADDRESS
Air Force Geophysics Laboratory
Hanscom AFB, Massachusetts 01731
Contract Monitor: Lt.Col. John D. Mill/OPA

12. REPORT DATE
August 1983

13. NUMBER OF PAGES
43

14. MONITORING AGENCY NAME & ADDRESS (if different from Controlling Office)

15. SECURITY CLASS. (of this report)
UNCLASSIFIED

15a. DECLASSIFICATION/DOWNGRADING SCHEDULE

16. DISTRIBUTION STATEMENT (of this Report)

Approved for public release; distribution unlimited.

17. DISTRIBUTION STATEMENT (of the abstract entered in Block 20, if different from Report)

18. SUPPLEMENTARY NOTES

19. KEY WORDS (Continue on reverse side if necessary and identify by block number)

Atmospheric Attenuation Coefficient
Atmospheric Optical Properties
Directional Sky and Terrain Radiance
Single Scattering Phase Function
Spectral Contrast Transmittance
Target Detection
Visible Image Transmission

20. ABSTRACT (Continue on reverse side if necessary and identify by block number)

The development of field oriented techniques for determining the atmospheric effects on visible image transmission are described in this report. Simplified analytic methods are presented for calculating the background sky, cloud and terrain radiance distribution, and in turn the spectral contrast transmittance, of inclined paths of sight in the atmosphere. The directional path radiance is determined as the

DD FORM 1 JAN 73 1473 EDITION OF 1 NOV 65 IS OBSOLETE
S/N 0102-014-6601

UNCLASSIFIED

SECURITY CLASSIFICATION OF THIS PAGE (When Data Entered)

20. ABSTRACT continued:

sum of the singly scattered sunlight component and a multiply scattered diffuse component that is calculated through application of the delta-Eddington approximation. Performance tests of the model radiance calculations were carried out through comparisons with results from more comprehensive radiative transfer models and by direct comparisons with high-resolution scanning radiometer measurements gathered by instrumented aircraft in a broad range of environmental conditions. Techniques for the representation of the optical parameters required as model input data are presented and discussed, including the specification of cloud optical depth as a function of cloud type.

An added feature of the contrast transmittance modeling system deals with the combined influences of atmospheric and target factors in order to calculate visual detection range for objects located at the surface and viewed from aloft. Analytic representations of vision experiment data are added along with target information to explore the relative sensitivity of detection range to selected changes in target and atmospheric parameters. Results are presented for several examples assuming simplified targets and backgrounds.

AFGL-TR-83-0236 **SIO Ref. 84-6**

ANALYTIC TECHNIQUES FOR ESTIMATING VISIBLE IMAGE TRANSMISSION PROPERTIES OF THE ATMOSPHERE

Wayne S. Hering

Visibility Laboratory
University of California, San Diego
Scripps Institution of Oceanography
La Jolla, California 92093

Approved:
RW Austin
Roswell W Austin, Director
Visibility Laboratory

Approved
William A. Nierenberg
William A Nierenberg, Director
Scripps Institution of Oceanography

CONTRACT NO. F19628-82-C-0060
Project No. 7670
Task No. 7670-14
Work Unit No. 7670-14-02

Scientific Report No. 3
August 1983

Contract Monitor
Lt. Col. John D. Mill, Atmospheric Optics Branch, Optical Physics Division

Approved for public release; distribution unlimited.

Prepared for

AIR FORCE GEOPHYSICS LABORATORY
AIR FORCE SYSTEMS COMMAND
UNITED STATES AIR FORCE
HANSCOM AFB, MASSACHUSETTS 01731

SUMMARY

The development of field oriented techniques for determining the atmospheric effects on visible image transmission are described in this report. Simplified analytic methods are presented for calculating the background sky, cloud and terrain radiance distribution, and in turn the spectral contrast transmittance, of inclined paths of sight in the atmosphere. The directional path radiance is determined as the sum of the singly scattered sunlight component and a multiply scattered diffuse component that is calculated through application of the delta-Eddington approximation. Performance tests of the model radiance calculations were carried out through comparisons with results from more comprehensive radiative transfer models and by direct comparisons with high-resolution scanning radiometer measurements gathered by instrumented aircraft in a broad range of environmental conditions. Techniques for the representation of the optical parameters required as model input data are presented and discussed, including the specification of cloud optical depth as a function of cloud type.

An added feature of the contrast transmittance modeling system deals with the combined influences of atmospheric and target factors in order to calculate visual detection range for objects located at the surface and viewed from aloft. Analytic representations of vision experiment data are added along with target information to explore the relative sensitivity of detection range to selected changes in target and atmospheric parameters. Results are presented for several examples assuming simplified targets and backgrounds.

TABLE OF CONTENTS

LIST OF TABLES AND ILLUSTRATIONS

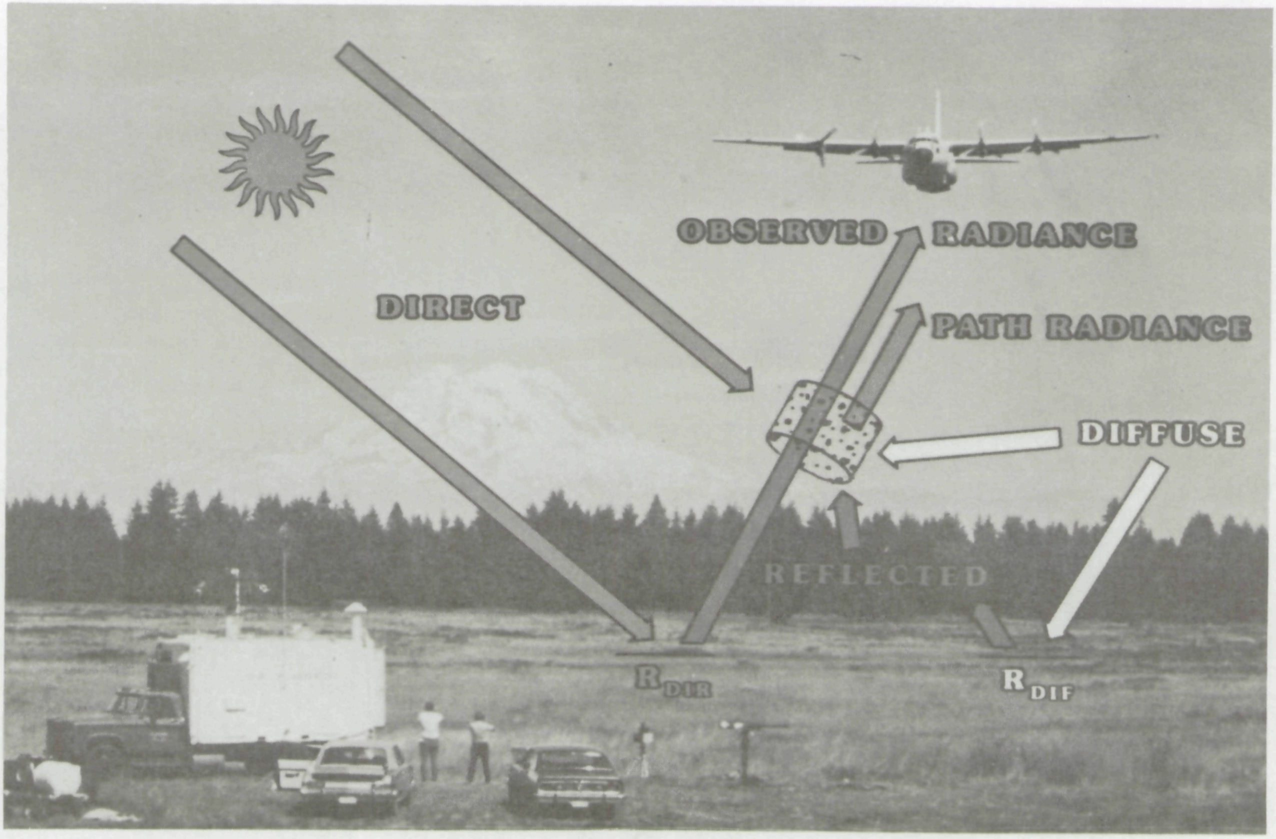

Frontispiece

The analytic techniques described in this report are a natural extension to a broad program of research into the optical properties of the atmosphere carried out by the Visibility Laboratory, University of California, San Diego, in cooperation with and under the sponsorship of the Air Force Geophysics Laboratory. The composite photograph shown above, illustrates some elements of the field program and some of the important components of the radiance field as measured by the instrumented aircraft. The field site near Mt. Rainier, Washington, is one of many locations in the United States and Europe where simultaneous measurements of optical and meteorological variables were gathered. Extensive high resolution measurements of the upper and lower hemisphere spectral radiance fields for scenes such as those illustrated by the fisheye camera photographs shown below (flight C-359) were of prime importance both for algorithm development and for validation of the modeling techniques over a wide range of environmental conditions.

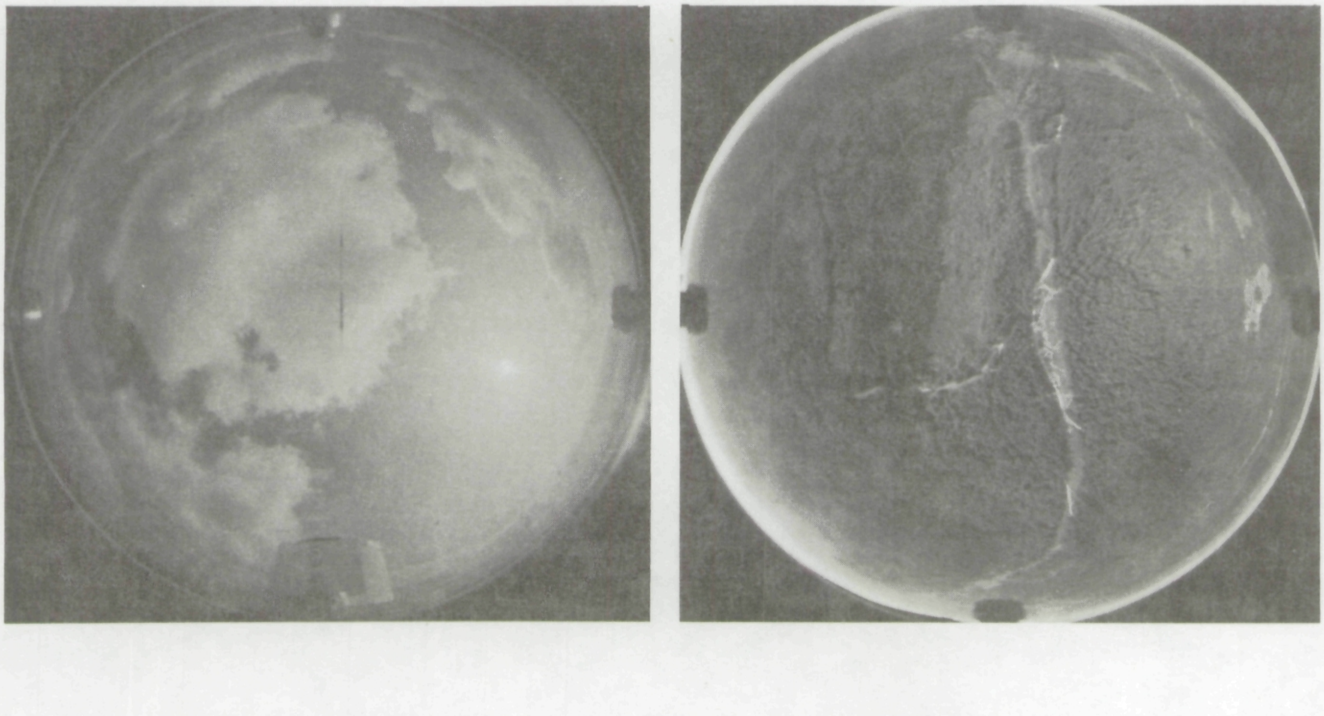

ANALYTIC TECHNIQUES FOR ESTIMATING IMAGE TRANSMISSION PROPERTIES OF THE ATMOSPHERE

Wayne S. Hering

1.0 INTRODUCTION

As set forth by Duntley (1948), the degradation of visible image contrast along a viewing path of increasing length is governed by (1) the attenuation of the inherent background and object radiances by air molecule and aerosol particle scattering and absorption, and (2) the generation of path radiance by molecular and aerosol scattering of incident light into the path of sight. Direct field measurements of the basic optical properties required for the determination of these factors for selected path segments cannot be made simply and inexpensively. Thus, operational estimates of contrast transmittance must be derived from model simulations that relate the aerosol directional scattering and absorption properties to generally available meteorological observations and forecasts (*e.g.* Shettle and Fenn, 1979). Additional problems stem from the complexity of multiple scattering processes and the relatively large amount of computer time and capacity required for treating the radiative transfer calculations completely as a physical problem. Effective simplifications must be made to yield fast yet consistent calculations of the radiance distribution. The successful development of techniques for real time estimates of the atmospheric effects on visible image transmission requires a reasonable balance between the desired accuracy, the complexity of the modeling procedures, and the reliability and representativeness of the available input data. Since these factors may vary considerably from one application to the next, it is important to retain reasonably good flexibility and completeness in the analytic approximations used for the estimates.

The development and testing of field oriented techniques for calculating directional path radiance and the object-background contrast transmittance along inclined paths of sight in clear-hazy atmospheres were described in a previous report (Hering, 1981). This paper addresses extensions and refinements to the modeling procedures and their validation. In particular, techniques are presented for (1) estimating the background radiance and visible image transmission characteristics in overcast sky conditions from conventional observations or forecasts of cloud type and altitude. As in the case of prior studies, technique development was based extensively on experimental data, including a broad series of simultaneous optical and meteorological measurements gathered with a specially instrumented aircraft. The high resolution profile measurements were obtained over a period of several years in a wide range of meteorological and geographical conditions in the United States and western Europe.

Further extensions of the modeling concepts deal with the combined effects of both environmental and target factors on visual detection range. Although independent assessment can be made of the changes in contrast transmittance that are associated with natural changes in the relevant atmospheric variables, the impact of these changes on target detection distance depends markedly on such factors as inherent target contrast, target size, and glimpse time. Analytic representations of vision experiment data (Blackwell, 1946 and Taylor, 1964) were added to the contrast transmittance model to explore the relative sensitivity of visual detection distance to a selected range of target and atmospheric variables. Results are presented for several examples assuming simplified targets and backgrounds.

A review of the basic equations and a summary of the analytic approximations used for calculating path radiance and for estimating visible spectrum contrast transmittance in cloudless atmospheres are given in Section 2. Also presented in Section 2, are comparative radiative transfer calculations between the simplified model and more complete computational methods. In Section 3, techniques are presented for the representation of the input variables that are required for the calculation of background radiance and spectral contrast transmittance. Extension of the modeling concepts to deal with image transmission characteristics for viewing paths below an overcast cloud layer are described in Section 4. Results of validation tests comparing model calculations with experimental measurements of the directional radiance distribution gathered by instrumented aircraft are given in Section 5. The results of sensitivity analyses which give a measure of the relative importance of individual target and environmental factors on the determination of target detection range are summarized in Section 6.

2.0 THEORY AND ANALYTIC APPROXIMATIONS

Although some refinements and additions to cloudless-sky modeling procedures are presented, this section is primarily a review of theory and analytic approximations given in Hering (1981).

Neglecting turbulence effects, the equation for the apparent spectral radiance of the background b at range r along the path of sight specified by zenith angle θ and azimuthal angle ϕ, can be written (Duntley *et al.* 1957)

$$ {}_bL_r(z,\theta,\phi) = T_r(z,\theta)\,{}_bL_o(z_t,\theta,\phi) + L_r^*(z,\theta,\phi)\ , \qquad (1) $$

where ${}_bL_o$ is the inherent background radiance at target altitude z_t,

$$ T_r = \exp - \int_o^r \alpha(r)dr $$

is the path transmittance, α is the volume attenuation coefficient, and L_r^* is the path radiance produced by the scattering of light from the sun and from the surrounding sky, clouds and terrain into the path of sight.

The path radiance is given by

$$ L_r^*(z,\theta,\phi) = \int_o^r L_*(z',\theta,\phi)T_r(z',\theta)dr'\ , \qquad (2) $$

where $L_*(z',\theta,\phi)$ is the path function, defined as the point function component of path radiance generated by the directional scattering of light reaching that point of the path. The expression for the path function can be written in terms of its contributions from the scattering of solar (lunar) scalar irradiance ${}_s\epsilon(z)$ and from the scattering of sky and earth radiances $L(z,\theta',\phi')$ as follows (*e.g.* Gordon, 1969b):

$$ L_*(z,\theta,\phi) = {}_s\epsilon(z)\sigma(z,\beta_s) + \int_{4\pi} L(z,\theta',\phi')\sigma(z,\beta')d\Omega'\ , \qquad (3) $$

where $\sigma(z,\beta)$ is the directional volume scattering function at angle β between the path of sight and direction of the source light, $d\Omega$ is an element of solid angle, and β_s is the scattering angle with respect to the sun.

In turn, the spectral contrast transmittance of the path of sight can be expressed (see Duntley *et al.* 1957) directly as the product of the path transmittance, $T_r(z,\theta)$, and the ratio of the inherent, ${}_bL_o$, and apparent, ${}_bL_r$, background radiances as follows:

$$ C_r(z,\theta,\phi)/C_o(z_t,\theta,\phi) = T_r(z,\theta)\,{}_bL_o(z_t,\theta,\phi)/{}_bL_r(z,\theta,\phi) \qquad (4) $$

where $C_r = ({}_tL_r - {}_bL_r)/{}_bL_r$ is the apparent target contrast at path length r, $C_o = ({}_tL_o - {}_bL_o)/{}_bL_o$ is the inherent target contrast at altitude z_t and ${}_tL_o$ is the inherent target radiance. Thus, the contrast transmittance of a given path does not depend upon intrinsic target characteristics but is a function only of the directional radiance distribution in the atmosphere and the path transmittance. The expression is strictly applicable only for monochromatic radiation but may be applied with good approximation to reasonably broad spectral bands in the visible portion of the spectrum.

From Eq. (3) we note that the path function and in turn the contrast transmittance as calculated from Eq. (4) depend upon the direction of the viewing path relative to the distribution of light reaching the path. The first term on the right hand side of Eq. (3) is the contribution of primary scattering of direct solar irradiance. The directional volume scattering function may be expressed

$$ \sigma(z,\beta) = P(z,\beta)s(z)\ , \qquad (5) $$

where $s(z)$ is the total volume scattering coefficient, and $P(z,\beta)$ is the single scattering phase function for combined Rayleigh plus aerosol particle scattering (see discussion in Section 3.3), which defines the probability that incident radiation will be scattered in the direction given by scattering angle β. The phase function varies significantly with the scattering properties of the aerosol particle distribution in the atmosphere.

Substituting Eq. (5) in Eq. (3), the expression for $L_*(z,\theta,\phi)$ becomes

$$ L_*(z,\theta,\phi) = {}_s\epsilon(z)P(z,\beta)s(z) + \int\int_{4\pi} L(z,\theta',\phi')P(z,\beta)s(z)d\Omega'\ . \qquad (6) $$

Modelling techniques for the calculation of the diffuse component of the path function are discussed in the following paragraphs.

2.1 Calculation of the Path Function

The second term on the right hand side of Eq. (6) is the component of the path function resulting from the scattering of diffuse radiance reaching the path from the surrounding sky and terrain. It has a directional dependence due to the asymmetry in the background sky and earth radiance distribution and the scattering phase function asymmetry. Precise numerical calculation of the path radiance resulting from the complex multiple scattering processes requires large amounts of computer time. For this reason, rapid approximate methods are employed extensively for radiation transfer calculations. The appropriate choice of computational method from among the variety of available methods depends upon the results desired for the application at hand.

While it is important to retain complete directionality for calculation of the path radiance component due to single scattering of direct solar radiance, approximate hemispherical two stream methods can be used effectively for fast calculation of the path radiance component due to scattering of the background sky and terrain radiances at any point and direction provided that the asymmetric influence of the prominent forward scatter peak and the irradiance profile are managed adequately. The delta-Eddington approximation introduced by Joseph, Wiscombe and Weinman (1976) satisfies the requirement. It extends the standard Eddington approximation, which assumes a simple cosine dependence of the single scattering phase function, through approximation of the phase function, P_d, by a truncated forward scatter peak and a two-term phase function expansion,

$$4\pi \, P_d(\beta) = 2f'\Delta(1-\cos\beta) + (1-f')(1+3g'\cos\beta) \qquad (7)$$

where f' is the fractional scattering represented by the forward peak and g' is the asymmetry factor of the truncated phase function. In effect, the delta-Eddington approximation transforms most of the enhanced radiance in the solar aureole into the direct solar flux component, and it is generally assumed that

$$f'(z) = g^2(z) \, . \qquad (8)$$

This assumption is commensurate with representation of the actual phase function with a single term Henyey-Greenstein phase function. Alternate expressions are required (see McKellar and Box, 1981) for other phase function representations such as the 2-term Henyey-Greenstein functions. Joseph *et al.* (1976) show that calculations of radiative transfer with the delta-Eddington approximation can be carried out with the standard Eddington computer code (Shettle and Weinman, 1970) with the following changes of variable

$$\Delta\tau' = (1-\omega f')\,\Delta\tau \, , \qquad (9)$$

$$\omega' = \omega(1-f')\,/\,(1-\omega f') \, , \qquad (10)$$

and

$$g' = (g-f')\,/\,(1-f') \, , \qquad (11)$$

where $\Delta\tau$ is the optical thickness of the layer and ω is the single scattering albedo.

As an integral part of the technique for estimating directional contrast transmittance, the products of the Eddington computer program (Shettle and Weinman, 1970) are used directly to calculate the second term on the right hand side of Eq. (6).

From the standard Eddington approximation, the diffuse radiance is assumed to be given by

$$L(z,\theta',\phi') = L_D(z) + L_{D'}(z)\cos\theta' \, . \qquad (12)$$

As shown by Shettle (1981), if we substitute Eq. (12) and the delta-Eddington approximations given by Eq. (7), (8) and (11) into the last term of Eq. (6) and integrate over θ' and ϕ', we have

$$\int\!\!\int_{4\pi} L(z,\theta',\phi')P(z,\beta)s(z)d\Omega$$

$$= s(z)\,[L_D(z) + gL_{D'}(z)\cos\theta] \, . \qquad (13)$$

A recent refinement in the above expression for the diffuse component of the path function consists of an additional term to help account for the effects of the azimuthal asymmetry in the background sky-terrain radiance distribution. The term is introduced as a rough approximation to an iteration of the singly scattered sunlight component of the path function. Its magnitude is assumed proportional to the single scattering component, ${}_s\epsilon(z)P(z,\beta)$, and proportional to the fractional contribution of the total diffuse energy, $4\pi\, L_D(z)$, to the sum of the total diffuse energy and singly scattered sunlight component at the level of computation. In other respects, the modification conforms with the extension of the delta-Eddington model introduced by Davies (1980); in particular, the contribution of the asymmetry term is proportional to $\sin\theta$, $\sin\theta_s$ and $\cos\phi$. The modified expression for the diffuse component of the path function is

$$\int\!\!\int_{4\pi} L(z,\theta',\phi')P(z,\beta)s(z)d\Omega$$

$$= s(z)\,[L_D(z) + gL_{D'}(z)\cos\theta + gL_{D''}(z)\cos\phi] \, , \qquad (14)$$

where

$$L_{D''}(z) = \frac{4\pi\, L_D(z)P(z,\beta)\,{}_s\epsilon(z)\sin\theta_s\sin\theta}{4\pi\, L_D(z) + P(z,\beta)\,\epsilon_s(z)} \, . \qquad (15)$$

Commensurate with the delta-Eddington approximations and Eq. (9), the expression for the solar scalar irradiance at altitude z is

$${}_s\epsilon(z) = {}_s\epsilon(\infty)\exp(-\tau_x\,/\,\cos\theta_s) \, , \qquad (16)$$

where ${}_s\epsilon(\infty)$ is the extraterrestrial solar scalar irradiance. The optical depth τ_x is assumed equal to the delta-Eddington optical depth, τ', everywhere except within the forward peak ($\beta < 25$ deg) where τ_x is equal to the unmodified value of τ. Substituting Eqs. (13) and (14) into Eq. (6), the expression for the path function becomes

$$L_*(z,\theta,\phi) = s(z)\,[P(z,\beta_s)\,{}_s\epsilon(\infty)\exp(-\tau_x\,/\,\cos\theta_s)$$

$$+ L_D(z) + gL_{D'}(z)\cos\theta + gL_{D''}(z)\cos\phi] \, . \qquad (17)$$

2.2 Calculation of Sky and Terrain Radiance

For an assumed plane parallel and horizontally homogeneous atmosphere, the directional path radiance, $L_r^*(z,\theta,\phi)$, and the radiance, $L(z,\theta,\phi)$, can now be calculated from Eqs. (1), (2) and (17) through finite summation over adjacent atmospheric layers using the trapezoidal rule. For upward paths of sight, the inherent background radiance of clear sky at target altitude is given by

$${}_bL_o(z_t,\theta,\phi) = L_\infty^*(z_t,\theta,\phi) \, , \qquad (18)$$

where $L_\infty^*(z_t,\theta,\phi)$ is the path radiance as determined at altitude z_t for the slant path from the top of the atmosphere to z_t. Looking downward, the inherent background radiance for the case of uniform Lambertian reflectance and a horizontal surface is given by

$$ {}_bL_o(z_t,\theta,\phi) = T_{ro}(z_t,\theta)R(\theta,\phi)E(0,d)/\pi + L_{ro}^*(z_t,\theta,\phi)\ , \qquad (19) $$

where $R(\theta,\phi)$ is the local surface reflectance, $E(0,d) = \epsilon_s(0)\cos\theta_s + \pi[L_D(0) + 2/3L_{D'}(0)]$ is the downwelling irradiance at the surface, and T_{ro} is the transmittance of the slant path from the surface to target altitude z_t.

2.3 Comparisons with Other Model Calculations

Tests were carried out to evaluate the performance of the simplified model for the radiance calculations as described above. Model calculations of radiance distributions were compared with the results calculated from more comprehensive radiative transfer models, which are mathematically precise but in general require relatively large computer capacity and time for the radiative transfer calculations. For these tests, the comparative accuracy was determined under the assumption that the physical system is perfectly observed, and the input data are identical for the approximate operational model and the comprehensive numerical models. The set of examples used for the analysis were selected from those proposed by the ad hoc Working Group of the Radiation Commission, International Association of Meteorology and Atmospheric

Table 1. Summary of numerical comparison cases listed in the Working Group Report (Lenoble, 1977) of the Radiation Commission, IAMAP, for 5 reference atmospheres.

Case	Atmosphere	Optical Thickness	Single Scattering Albedo	Solar Zenith Angle
1	Haze L	1	1.0	0°
2	Haze L	1	0.9	0°
3A	Haze L (ϕ = 0°)	1	0 9	60°
3B	Haze L (ϕ = 90°)	1	0.9	60°
3C	Haze L (ϕ = 180°)	1	0 9	60°
4	Cloud	64	1 0	0°
5	Cloud	64	0.9	0°

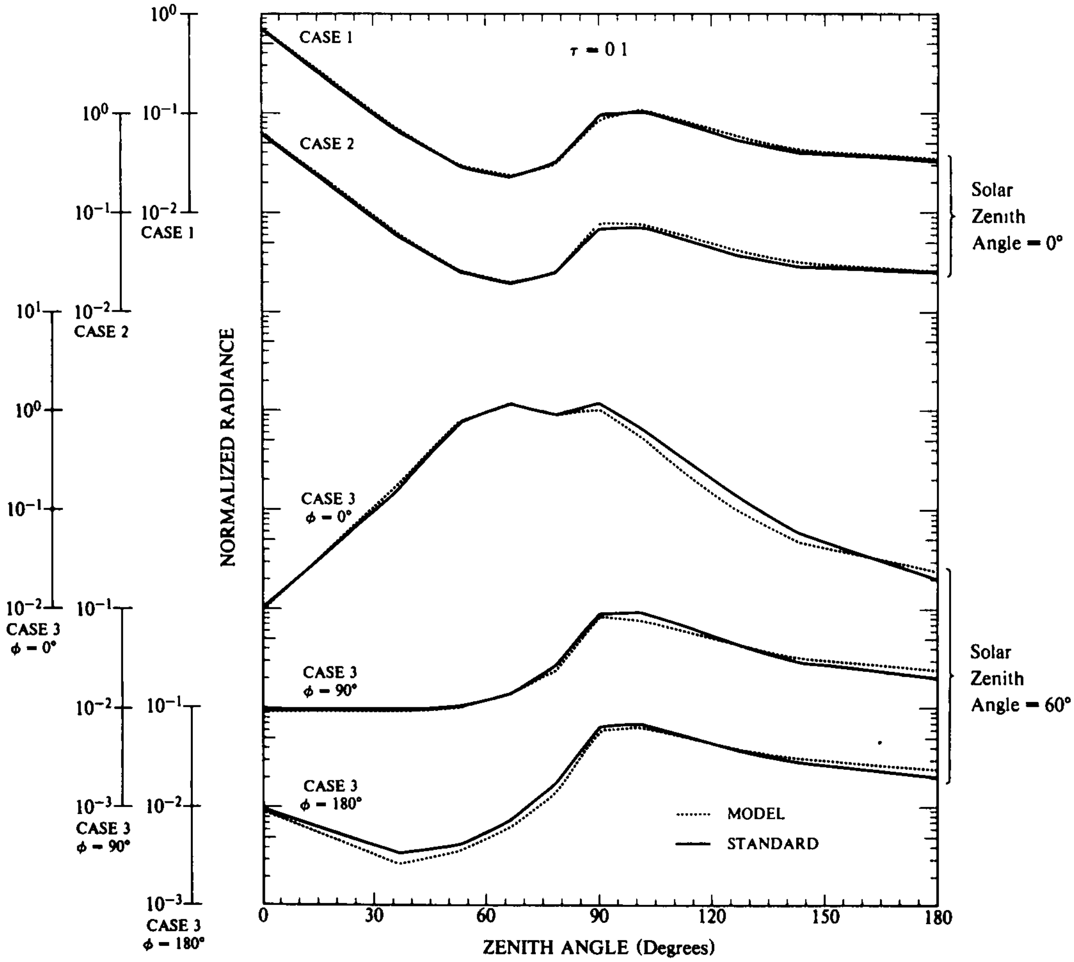

Fig. 1. Comparative radiance calculations for optical depth 0.1 for reference cases 1,2 and 3. Model results (dashed lines) are compared with the spherical harmonics method, (Lenoble, 1977), (solid lines). Optical parameter data for each case are given in Table 1.

Physics (Lenoble, 1977, see Table 1). The results of the spherical harmonic method listed in the Working Group report were chosen for a reference standard since comparative calculations using this method were presented for all five test cases. A single layer, plane parallel and homogeneous atmosphere with a black underlying surface was prescribed in each case. Three cases have a Haze L (Deirmendjian, 1969) aerosol particle distribution with an optical thickness of 1, and the other two have assumed cloud particle distributions with an optical thickness of 64. The phase function for single scattering and the single scattering albedo are specified for each case. Comparative results of the radiance calculations are illustrated in Figs. 1-4.

It is important to note that the agreement among the more rigorous numerical methods, as given in the Working Group report, is generally within a few percent depending upon the completeness of scattering history retained in the calculations. We see from Fig. 1 that the departures of the simplified model radiance calculations from the reference values for the haze cases are significantly larger, yet the indicated accuracy is good when considered in context with the uncertainties and completeness of the observational data base from which the estimates must be derived in operational practice. The simplified model requires only a few seconds of large scale computer time for each case, and the model is designed for easy microprocessor application for real time requirements. The approximations inherent in the computationally fast model serve to smooth out the asymmetry in the calculated radiance component due to the scattering of incident diffuse light; hence it is expected that the error of estimate would continue to increase somewhat in the solar azimuthal plane (ϕ = 0–180 deg) as the solar zenith angle increases beyond 60°.

The relative effectiveness of the azimuthal asymmetry term, $g\ L_{D''}\cos\phi$, is illustrated in Table 2. Model calculations for Case 3 (θ_s = 60 deg, ω=0.9) are listed with and without the azimuthal component contribution for comparison with the reference model results. It is evident that the accuracy of Eq. (17) is much better with the azimuthal correction. However, systematic errors remain such that further study of this aspect of the modeling procedures is particularly important.

The relative performance of the model calculations of radiative transfer in a high extinction environment is illustrated in Figs. 3 and 4. Both of the cloud examples in the reference series assume an overhead sun position.

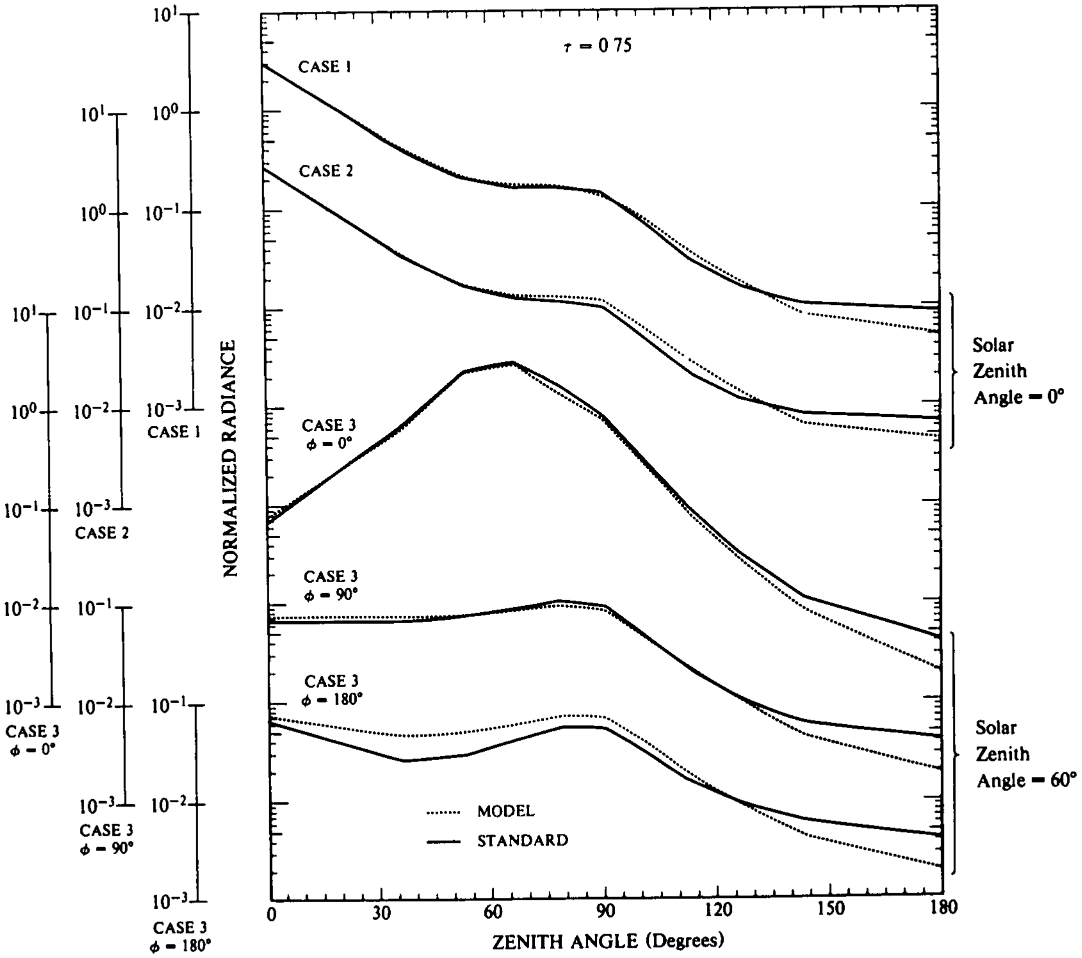

Fig. 2. Same as Fig. 1 except for 0.75 optical depth.

Table 2. Comparison of Case 3 radiance distributions as calculated by the Spherical Harmonics method (column SH), the simplified model without azimuthal asymmetry term (column A), and simplified model with the azimuthal asymmetry term (column B) The solar zenith angle is 60 deg Calculations are shown for a level near the top of the haze layer ($\tau = 0\ 1$) and a level near the base ($\tau = 0\ 75$) Note that the azimuthal term, $g\ L_{D''} \cos\phi$, is zero for $\phi=90$ deg, hence columns A and B are identical

$\tau = 0\ 1$

	$\phi=90°$		$\phi=0°$			$\phi=180°$		
μ	SH	A	SH	A	B	SH	A	B
1	1 01-2	9 58-3	1 01-2	9 58-3	9 58-3	1 01-2	9 58-3	9 58-3
8	9 50-3	9 43-3	1 65-1	1 66-1	1 82-2	3 50-3	3 84-3	2 79-3
6	1 04-2	1 04-2	7 78-1	7 50-1	7 84-2	4 30-3	5 29-3	3 79-3
4	1 42-2	1 38-2	1 17-0	1 11-0	1 17-0	7 46-3	9 14-3	6 55-3
2	2 75-2	2 42-2	9 07-1	7 90-1	8 89-1	1 78-2	2 00-2	1 43-2
- 2	9 11-2	7 72-2	6 50-1	3 80-1	5 30-1	6 92-2	8 51-2	6 47-2
- 4	6 56-2	5 92-2	3 08-1	1 59-1	2 21-1	5 11-2	6 40-2	5 10-2
- 6	4 32-2	4 36-2	1 36-1	7 52-2	9 78-2	3 72-2	4 84-2	3 92-2
- 8	2 87-2	3 24-2	5 74-2	4 04-2	4 75-2	2 83-2	3 84-2	3 21-2
-1 0	2 00-2	2 47-2	2 00-2	2 47-2	2 47-2	2 00-2	2 47-2	2 47-2

$\tau = 0\ 75$

	$\phi=90°$		$\phi=0°$			$\phi=180°$		
μ	SH	A	SH	A	B	SH	A	B
1	6 73-2	7 64-2	6 73-2	7 64-2	7 64-2	6 73-2	7 64-2	7 64-2
8	6 69-2	7 53-2	6 79-1	5 25-1	6 10-1	2 61-2	5 16-2	4 71-2
6	7 38-2	7 72-2	2 30-0	2 00-0	2 21-0	3 00-2	5 77-2	5 19-2
4	8 82-2	8 44-2	2 78-0	2 39-0	2 68-0	4 13-2	6 97-2	6 13-2
2	1 05-1	9 44-2	1 61-0	1 03-0	1 30-0	5 56-2	8 59-2	7 34-2
- 2	4 41-2	4 36-2	2 66-1	1 66-1	2 39-1	2 92-2	4 68-2	3 48-2
- 4	1 94-2	2 03-2	8 41-2	5 12-2	7 20-2	1 48-2	2 18-2	1 77-2
- 6	1 00-2	1 02-2	2 95-2	1 89-2	2 53-2	8 96-3	1 15-2	8 97-3
- 8	5 98-2	4 67-2	1 10-2	6 73-3	8 60-3	6 24-3	6 23-3	4 57-3
-1 0	4 02-3	2 14-3	4 02-3	2 14-3	2 14-3	4 02-3	2 14-3	2 14-3

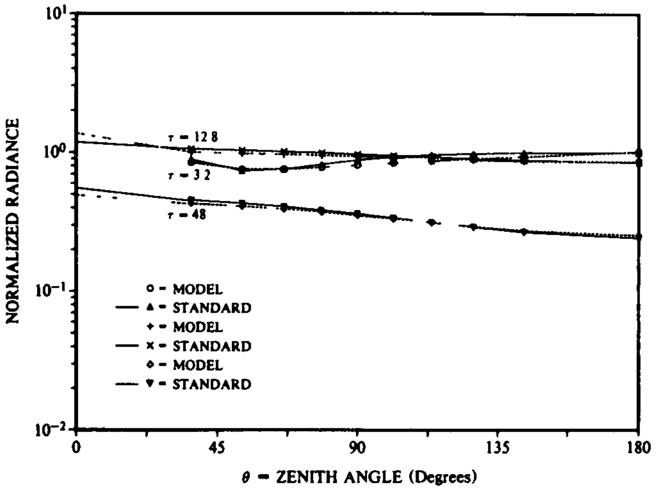

Fig. 3. Same as Fig. 1 except for cloud case 4 at optical depths 3.2, 12.8, and 48 and no absorption.

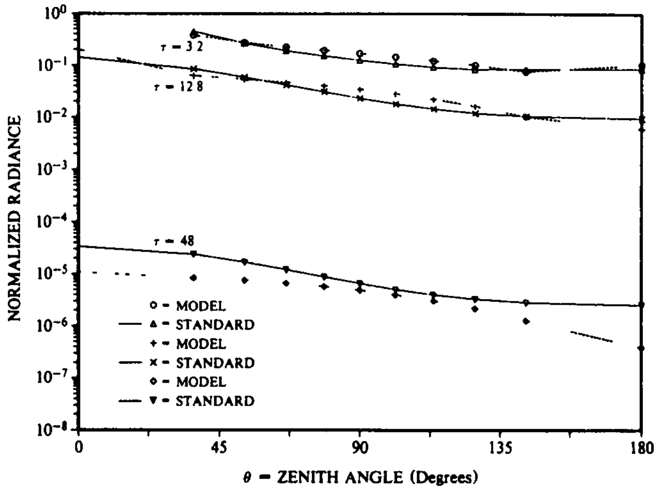

Fig. 4. Same as Fig. 3 except for cloud case 5 with single scattering albedo of 0.9.

Tne agreement with the reference model calculations holds well for both cloud cases, although the disparity increases with increasing depth for the case with strong absorption. The simplified model calculations of in-cloud radiance were carried out through division into sub-layers with boundaries corresponding to levels where reference model calculations were available. These subdivisions represent large increments of optical depth in the cloud cases. However, the estimates if in-cloud radiance are good in general over the full range of optical depth and observing angles shown in Fig. 3 and 4. A notable exception is for the data point directly upsun, $\theta=\theta_s=\phi=0$, at optical depth 3.2. The calculated values of in-cloud radiance for this data point result in overestimates by at least an order of magnitude and plot offscale in Figs. 3 and 4. The modeling procedures require important refinement in layer by layer resolution in order to handle combined effects of the rapid attenuation of the direct solar beam in the cloud near the upper limit of the cloud layer and the strong change in the single scattering phase function with scattering angle for β less than 5 deg. The large errors are confined to viewing paths within a few degrees of the sun and to the region near upper limit of the cloud layer. In this region, the singly scattered sunlight component makes a significant contribution to the path function and it changes rapidly along the path.

3.0 APPLICATION OF ANALYTIC TECHNIQUES

Environmental data and forecasts relevant to the determination of the background spectral radiance distribution and image transmission characteristics may be available in many forms and with varying degrees of completeness and representativeness. Emphasis has been placed on the development of a general modular format for requisite data entry seeking to take full advantage of all available information important for a particular application of the radiance model. A summary of input variables and alternate techniques for the specification of the atmospheric properties are included in Appendix A. Basic data entries include the wavelength representative of the sensor spectral characteristics, solar zenith angle, and the observational paths of interest for the problem at hand. Specification of the underlying surface reflectivity is discussed below in Section 3.1.

Several options are available for the input of specific atmospheric variables. One may introduce as many atmospheric layers as warranted by the accuracy and completeness of the meteorological observations or forecasts available for the specification of the optical parameter profiles. Minimum information for each designated layer includes the altitude limits, the average scattering coefficient, the average absorption coefficient and the single scattering phase function for aerosol particle scattering. Techniques for the representation of these variables are discussed in Sections 3.2 and 3.3.

3.1 Representation of Surface Reflectance

The background surface reflectance contributes to the calculated radiance distribution in two ways. First, the general or broad area average surface reflectance is entered to calculate the component of path radiance that is generated by light reaching the path through scattering from the underlying surface and in turn scattered in the direction of the sensor as given by Eq. (6). For a land surface, the reflectance is assumed to conform with Lambert's law, so that the resultant radiance is independent of observation angle and depends only on the downwelling irradiance and the average surface reflectance.

Second, the local background reflectance, which may differ from the area averaged reflectance discussed above, is entered for the determination of the inherent background radiance and its contribution to the apparent spectral radiance as given by Eqs. (1) and (19).

The above algorithms deal with surface reflectance over land areas. Another option, for use primarily over an open water surface, assumes specular surface reflection. Here the surface radiance is a function of both the viewing angle and the downwelling radiance distribution. For the water option, the Fresnel reflectance of the water surface as a function of observation angle is set equal to average values for a sea surface roughened by light surface winds (4m sec^{-1}). These values as calculated by Gordon (1969a), assume that the crosswind and upwind wave slope probabilities of Cox and Munk (1954) may be approximated by a single circular distribution of wave slopes.

3.2 Representation of Total Volume Scattering Coefficient

The spatial distribution of total volume scattering coefficient deserves prime consideration since it is the major determinant of visible spectrum contrast transmittance. Techniques for the specification of the scattering coefficient profile have been investigated during the course of the aircraft measurement and analysis program. Some of the results of these studies and their application to operational modeling procedures were summarized by Hering (1981). A brief review is given here for immediate reference.

For profile modeling purposes, it is important to consider a conservative measure of scattering coefficient that in the absence of local aerosol particle sources or sinks does not change appreciably following the air motion. The optical scattering mixing ratio, $Q(z)$, is such a parameter. As the vertical mixing within an identifiable atmospheric layer becomes more complete, $Q(z)$ becomes more constant with height within the layer.

The optical scattering ratio is defined

$$Q(z) = s(z)/s_R(z)\ , \tag{20}$$

where $s_R(z)$ is the total volume coefficient for Rayleigh scattering at altitude z. Note that

$$s(z) = s_R(z) + s_M(z) = \omega(z)\alpha(z)\ , \tag{21}$$

where $\alpha(z)$ is the extinction coefficient and $s_M(z)$ is the aerosol scattering coefficient. It follows that the aerosol scattering ratio is given by

$$s_M(z)/s_R(z) = Q(z) - 1\,. \qquad (22)$$

The aerosol scattering ratio also would be constant under conditions of complete aerosol mixing. An additional computational advantage of a scattering ratio representation is that it provides normalization with respect to both density altitude and wavelength.

Profiles of $Q(z)$ derived from the extensive series of airborne optical measurements made by the Visibility Laboratory, reveal large variability depending upon the aerosol particle source strength and the nature of the convective and turbulent mixing processes. The problem is to model the essential characteristics of the $Q(z)$ profiles in a way that recognizes operational observing and forecasting limitations yet takes maximum advantage of existing capabilities. A prominent feature of the daytime aircraft soundings over inland areas was the marked tendency for $Q(z)$ to remain essentially constant with height within the boundary layer, and also in the relatively haze-free region of the upper troposphere above the primary haze layer. It should be emphasized that the assumption of constant scattering ratio with height does not hold well for ground-based stable layers with little vertical mixing such as those associated with the nocturnal formation of fog. However, for application to problems of contrast transmittance in hazy atmospheres in the daytime following the dispersion of any surface inversion existing at sunrise, a simple 3-layer troposphere model with constant $Q(z)$ in each layer provides in most cases a good first approximation of the aerosol scattering profile. Thus, the forecasting problem is reduced to the prediction of the upper altitude limit of mixed boundary layer and the average scattering ratio within each layer. An evaluation of model representations of the high resolution scattering ratio profiles as measured during several deployments of the instrumented aircraft in western Europe is given in Hering (1981).

Three examples of scattering coefficient profiles as measured by the integrating nephelometer are shown in Fig. 5. Each experimental flight usually included profile measurements with 4 spectral filters having peak wavelengths of 475, 550, 660, and 750 nm. The 4 profiles were measured sequentially over approximately a 2-hour period. Data for individual profiles were extracted at 30-m intervals. Figure 5 illustrates some recurrent features of the lower tropospheric profiles; the well mixed boundary layer in late morning and afternoon over inland areas of northern Europe (Soesterberg profile), the multi-structured profile in low-level fog conditions offshore near Rodby, Denmark, and the deep haze layer typical of the summer profiles measured in the Mediterranean Sea area (Trapani, Sicily).

Cursory analysis of a large number of simultaneous aircraft measurements of temperature and scattering coefficient profile structure indicate that a temperature lapse rate equal to the standard lapse rate of 6.5°C per km or greater will support rather complete vertical mixing of aerosol particles in the size range contributing predominantly to extinction in the visible portion of the spectrum. On the other hand, atmospheric layers of thickness greater than about 300 m and lapse rate less than about 4.5°C per km significantly inhibit vertical mixing and in general appear sufficient to cap the mixed boundary layer.

3.3 Representation of Single Scattering Phase Function and Single Scattering Albedo

The single scattering phase function $P(z,\beta)$ as employed in Eq. (6) is a bulk parameter of the atmos-

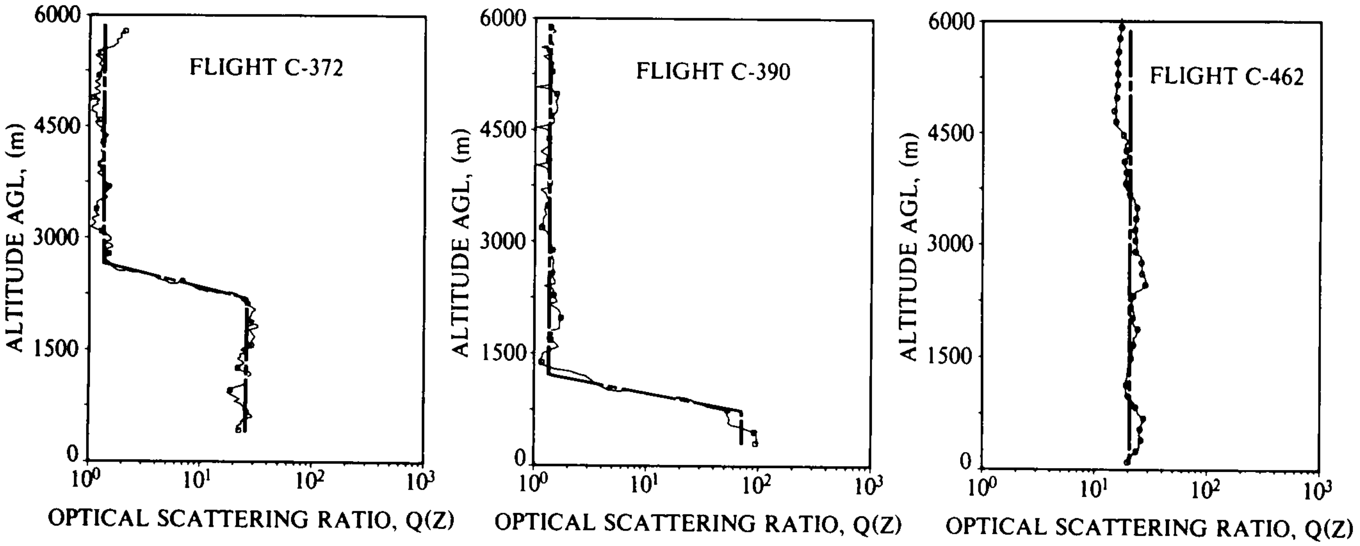

Fig. 5. Scattering ratio profiles as measured for flight C-372 (Soesterberg, Netherlands), flight C-390 (Rodby, Denmark) and flight C-462 (Trapani, Sicily). The heavy dashed line is an objective model representation of the profile. The spectral nephelometer measurements were corrected for the effects of incomplete purging of the instrument.

pheric layer, representing the combined aerosol and Rayleigh phase functions. It is given by

$$P(\beta,z) = \frac{P_R(\beta) + [Q(z) - 1]P_M(\beta,z)}{Q(z)} , \qquad (23)$$

where $P_M(\beta,z)$ is the phase function for aerosol scattering and the theoretical Rayleigh phase function is

$$P_R(\beta) = 3(1 + \cos^2\beta) / 16\pi . \qquad (24)$$

The phase function for single scattering has the normalized form,

$$\int_{4\pi} P(z,\theta,\phi) d\Omega = 1 . \qquad (25)$$

The computational scheme offers several options for specification of the average single scattering phase function $P(z,\beta)$, for each designated atmospheric layer. Detailed estimates of $P_M(\beta)$ available from prescribed aerosol models such as those associated with LOWTRAN (Shettle and Fenn, 1979), may be entered directly and used in a table look-up format. A second option is the representation of the aerosol phase functions by two-term Henyey-Greenstein functions (Irvine, 1968) as follows,

$$P_M(\beta,g_1,g_2,c) = c\,P_{HG}(\beta,g_1) + (1-c)\,P_{HG}(\beta,g_2) , \qquad (26)$$

where

$$P_{HG}(\beta,g) = (1-g^2) / [4\pi(1 - 2g\cos\beta + g^2)^{3/2}] , \qquad (27)$$

and the asymmetry factor, g, is given by

$$g = \frac{1}{2}\int_0^{\pi} P(\beta)\cos\beta \sin\beta \, d\beta . \qquad (28)$$

To the extent that the Henyey-Greenstein asymmetry factors, g_1 and g_2, and the partitioning factor, c, can be estimated from reference atmosphere calculations they can be entered for the specification of the required scattering phase functions. In the absence of information that may serve to identify the directional scattering properties of individual aerosol layers, yet another option may be used as described in Hering (1981). Empirical functions were developed which prescribe the Henyey-Greenstein function parameters, g_1, g_2, and c, as a function of the scattering ratio $Q(z)$. The derived expressions are based to a large extent on the average phase functions for selected ranges of scattering coefficient as measured by Barteneva (1960).

The other direct-entry variable for each designated atmospheric layer is the single scattering albedo, $\omega(z)$. It is defined by the expression

$$\omega(z) = s(z) / \alpha(z) . \qquad (29)$$

So that the fraction of radiation absorbed for each single photon collision is $1 - \omega(z)$. Commensurate with other variables, $\omega(z)$ is introduced as a bulk parameter and is a measure of the combined absorption effects of both air molecules and aerosol particles. In the visible spectrum, $\omega(z)$ in the boundary layer ranges from 1.0 (no absorption) to less than 0.7 in urban atmospheres with appreciable carbon concentration.

4.0 APPLICATION TO OVERCAST SKY CONDITION

The clear-sky modeling concepts and computational scheme can be applied in the same form to calculate the visible spectrum radiance fields and contrast transmittance for continuous cloud cover conditions. Given reliable empirical estimates of cloud optical properties, the delta-Eddington method yields good estimates of the irradiance profiles in overcast atmospheres. In turn, the directional path radiance fields and the contrast transmittance for selected slant paths may be calculated from the expressions given in Section 2. In practice, one must rely on cloud model estimates of the optical depth, the single scattering phase function, and the single scattering albedo as a function of standard cloud type.

4.1 Estimates of Optical Depth from Conventional Cloud Observations

Rough empirical approximations of the average optical depth as a function of cloud type were derived through reference to a climatological summary of the SOLMET (1977) data base as included in a report by Shapiro (1982). The SOLMET data base was compiled by the National Climatic Center under the sponsorship of the Department of Energy. It consists of a long record of edited and adjusted solar radiation data (hourly averages) for 26 National Weather Service stations spread throughout the United States coupled with the conventional hourly surface observations for these stations. The climatological tabulations of the broad-band solar irradiance were available in the form of averages for all stations and all seasons for standard cloud types (10/10 cloud cover) for selected solar zenith angles. These data were combined with the average irradiance data for cloudless skies to calculate the ratio of the average broad-band irradiance for the sky covered by clouds of specific types to the average broad-band irradiance for cloudless atmospheres.

It is important to note that the calculated overcast/clear irradiance ratios for different cloud types and solar angles derived from the SOLMET data base agree very closely with the average overcast/clear irradiance ratios calculated by (Haurwitz (1948)) for comparable cloud classifications using 8 years of observations at the Blue Hill Observatory in Massachusetts.

To the extent the fractional transmittance for the different cloud types as determined from the broad-band

(.295-2.8μm) pyronometer measurements are representative in general of the visible spectrum, one can use the delta-Eddington method to estimate the effective average optical depth associated with the individual cloud types. The results of trial calculations made to obtain rough estimates of the optical depth of standard cloud types are shown in Fig. 6. Through successive approximation, determination was made of the best least-squares fit between the average overcast/clear irradiance ratios as a function of solar zenith angle derived from the SOLMET data base and the corresponding values calculated with the delta-Eddington model. A central wavelength of 550 nm and an average surface reflectance of .07 were used for the model calculations and absorption within the cloud layer was assumed negligible. The altitude limits of the cloud layers were chosen so as to conform in general with typical values for each cloud type.

Except as noted below, the asymmetry factor, g, was assumed equal to .85 in calculations for all cloud types. It should be emphasized that the model calculations are sensitive to variations in g. However, in the case of water clouds, the variation in g is small (Twomey, 1980) and the resultant uncertainties are negligible in comparison with the natural variations in optical depth for each cloud type. In the case of ice clouds, very significant fluctuations in g are associated with variations in ice crystal size, shape, and orientation. For this reason, as emphasized by Welch, *et al.* 1980, attempts to estimate the optical depth of clouds composed of non-spherical particles from observed cloud reflectance (or transmittance) are subject to considerable error. For comparison purposes, estimates were derived for both a nominal value of .85 for the asymmetry factor in cirrus clouds and a marked reduction to .75. In agreement with the results of Welch, *et al.* 1980, the calculated optical depths corresponding to the same average cirrus cloud transmittance differ by more than a factor of 2 for the two assumed values of g as shown in Table 3.

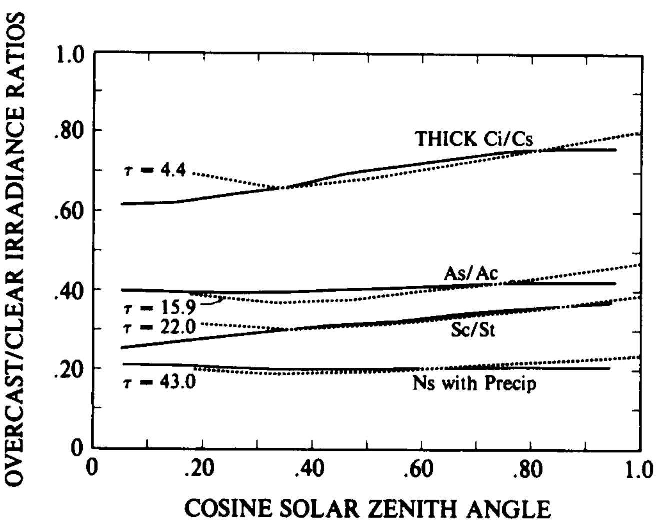

Fig. 6. Average overcast/clear irradiance ratios from SOLMET data base (solid lines) and estimated with delta-Eddington approximation (dashed lines). Listed are the values of optical depth, τ, giving the best correspondence.

Table 3.

The approximate average and ± standard deviation values of optical thickness for various cloud forms as calculated using the delta-Eddington approximation and the SOLMET data base. The assumed value of asymmetry factor is given in column g. For reference purposes a value of scattering ratio, Q(550nm), is shown for each value of $\Delta\tau$ as determined for a cloud of geometric cloud thickness of 1 km and a base altitude as indicated.

Cloud Type	Optical Thickness	Q(550 nm) $\Delta z = 1\,km$	Base Alt.(km)	g
St/Sc	22.0	2200	1 km	
	13.5	1350		.85
	41.0	4100		
Cu/Cb	15.0	1500	1 km	
	10.0	1000		.85
	26.5	2650		
As/Ac	15.9	1950	3 km	
	9.8	1200		.85
	25.3	3100		
Ns (precip.)	43.0	4300	1 km	
	20.7	2700		.85
	126	12600		
Ci/Cs (thick)	4.4	750	6 km	
	3.2	550		.85
	6.2	1050		
Ci/Cs (thin)	1.5	250	6 km	
	0.7	125		.85
	2.4	400		
Ci/Cs (thick)	2.6	440	6 km	
	1.5	250		.75
	4.3	725		
Ci/Cs (thin)	0.7	120	6 km	
	0.2	30		.75
	1.5	250		

As indicated by the examples in Fig. 6, one can obtain a rather close fit of the average irradiance ratios *vs* solar zenith angle for the standard cloud types using the delta-Eddington model. The optical depths corresponding to the closest approximations of the SOLMET data averages for each cloud type are listed in Table 2. Rough estimates of the variability in the optical depth were obtained in a similar manner from the SOLMET data. The tabulated values of optical depth labeled "± rms variation" were calculated from SOLMET irradiance ratios equal to the average ratio for a given cloud type and solar zenith angle plus and minus the root-mean-square departure of the individual SOLMET values of irradiance ratio from the averages for that cloud type.

Thus, for overcast sky conditions, the radiance field at any altitude may be calculated using the optical properties given in Table 2 corresponding to the observed cloud type and altitude and the estimated input variables for the additional atmospheric layers above and below the cloud layer. The optical scattering ratio for the cloud layer is given by the cloud optical depth divided by the Rayleigh optical depth for the corresponding altitude interval of the cloud. In view of the uncertainty in the asymmetry factor for cirrus cloud particle distributions, estimates for g equal to .75 are shown as well as for the more representative value of .85. In the absence of other information, operational use of the results for g=.85 are suggested.

Several comparisons of the calculated spectral radiance fields with the high resolution aircraft measurements for both clear and cloudy atmospheres are given in the following section.

5.0 COMPARISONS OF MODEL RESULTS WITH MEASURED DATA

From the fundamental Eq. 4, we note that the reliability of model calculations of slant-path contrast transmittance are dependent directly upon the accuracy with which the radiance fields $L_r(z, \theta, \phi)$ are determined. For this reason, continuing emphasis has been given to direct comparisons of the radiance fields as calculated by the modeling procedures and the corresponding radiance fields observed as part of the extensive airborne measurement program. The upper and lower scanning radiometers measured the apparent radiance fields surrounding the aircraft as it probed the lower troposphere up to an altitude of 6 km. The processed radiometer measurements provided data with 5-degree resolution in the 4 specific wavebands commensurate with the integrating nephelometer measurements of total volume scattering coefficient (peak wavelengths of 475, 550, 670 and 750 nm).

Several of the comparisons between model calculations and measured radiance fields are shown in Figs. 8 to 12. The plotted data are presented for either one of two vertical planes (0-180 deg or 90-270 deg) with respect to the solar azimuth and depict data sweeping from the nadir (θ = 180 deg) up through the horizon and zenith and then downward through the opposite horizon to nadir, as shown in Fig. 7. A series of examples were selected in order to illustrate model performance over a wide range of haze-layer extinction, solar zenith angle, and surface reflectance (land and sea) for both clear and overcast sky conditions.

The specific input data for each of the illustrated examples are listed in Appendix B. Except for the scattering mixing ratio profile in the lower troposphere, the other input variables were approximated by their average or climatological values. The scattering mixing ratio for the boundary layer was entered as determined directly from the nephelometer measurements for that particular flight profile. The scattering ratio for the upper troposphere and stratosphere during this period of minimal volcanic activity was held constant for all cases and set equal to a characteristic value of 1.2 at 550 nm. The mixing ratio for other wavelengths at upper levels was determined assuming the wavelength dependence of the aerosol scattering coefficient equal to $(\lambda/\lambda_{550})^{-1}$. The aerosol single scattering phase function for all haze layers and all cases was specified by a two-term Henyey-Greenstein function with parameters; g_1 = .714, g_2 = -.613, and c = .963. The corresponding values for the cloud layers are .890, -.660 and .980.

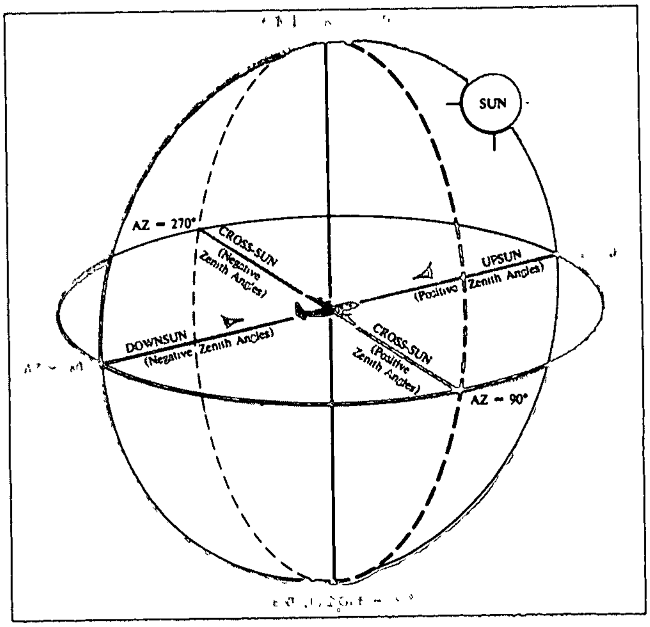

Fig. 7. Coordinate system for the calculation of sky and terrain radiance and slant-path contrast transmittance.

Optical depths for the overcast sky layers were specified equal to the average value for the observed cloud type as developed in Section 4 (see Table 2). The single scattering albedo and surface reflectance were assumed equal to average values for the prevailing conditions. For flights conducted over open water, the average Fresnel reflectance distribution for wind-ruffled sea (see Section 3.1) was used.

5.1 Comparative Results for Individual Flights

Flight C-379, Fig. 8, was a midday flight off the south coast of Lolland Island, Denmark. The example depicts the characteristic changes with altitude of the upper and lower hemisphere radiance fields under cloudless skies and light haze conditions. Note the characteristic uniformity and symmetry of the sea surface radiance fields in the cross-sun plane.

Flight C-466, Fig. 9, was conducted over open farmland and wooded areas in northwestern Germany. Scattered cirrus clouds and isolated patches of altocumulus were observed. A layer of moderate haze extended to an altitude of 1350m. Notice the marked fluctuations in the observed apparent terrain radiance associated with variations in ground cover (green and brown fields and dark

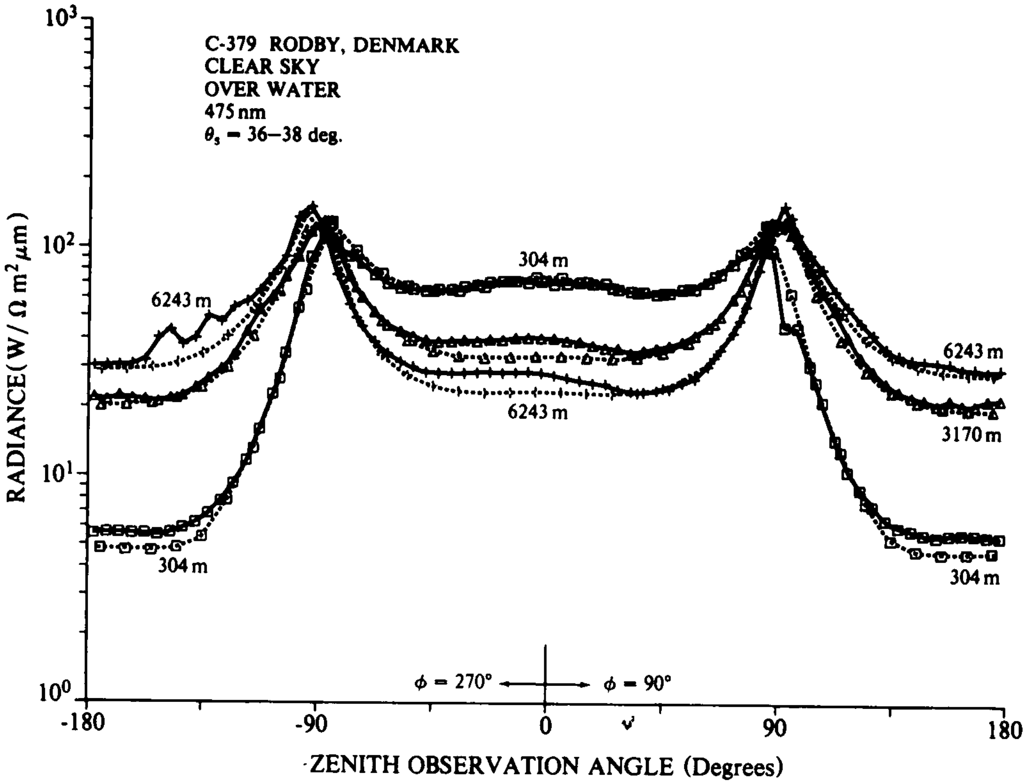

Fig. 8. Comparison of sky and terrain radiance as measured by airborne scanning radiometer (Johnson 1981d) (solid line) and model calculations (dashed line).

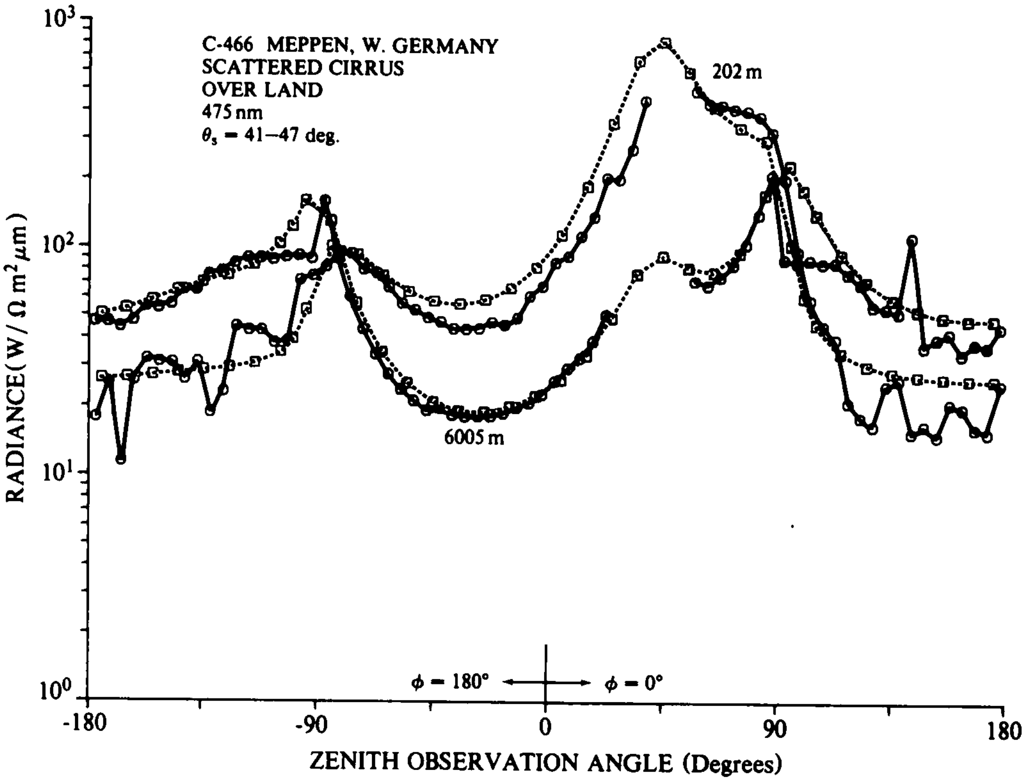

Fig. 9. Comparison of sky and terrain radiance as measured by airborne scanning radiometer (Johnson 1981d) (solid line) and model calculations (dashed line).

woods), as opposed to the smooth terrain radiance distribution calculated with the assumption of uniform Lambertian surface reflectance.

Flight C-469, Figs. 10 and 11, was an afternoon flight over open farmland in central Netherlands. The examples illustrate the variations in radiance fields with altitude in dense haze conditions. Depicted also are the characteristic differences in the radiance distributions as observed in the narrow blue passband (475 nm) as shown in Fig. 10 and in the near infrared passband (750 nm) shown in Fig. 11. Note in particular the reduction in overhead sky radiance at 750 nm associated with diminished molecular and aerosol particle scattering and the enhanced apparent terrain radiance due to the greater surface reflectance in the near infrared portion of the spectrum.

Flight C-401, Fig. 12, was a winter day flight with low sun elevation over a rural area in northwestern France. Scattered cumulus and scattered thin cirrus clouds were observed with a layer of light haze extending to an altitude of about 1 km. The relatively bright horizon in contrast with low overhead sky and terrain radiance is a prominent feature of low-sun radiance fields. As indicated by this example, the good agreement between model calculations and measured radiance fields characteristically found in the comparisons extends to the cases with low solar elevation angle.

Flight C-422, Fig. 13, is also an over water flight off the coast of Denmark, but on this day the sky was overcast with stratocumulus clouds having a base altitude of 1800m. Heavy haze was present at all levels below the cloud base. The example illustrates the highly symmetric and uniform distribution of cloud and sea radiance typical of measurements made with the flight path over open water and under an overcast cloud layer.

Flight C-465, Fig. 14, was an afternoon flight in mid summer over northwestern Germany. The sky was overcast with stratocumulus clouds having a base altitude of 1600m. A layer of light haze was observed below the cloud base. In contrast to the previous case, the radiance field was more irregular in structure due to the variations in cloud optical thickness and to the variations in ground cover reflectivity.

Flight C-435, Fig. 15, was a winter flight over a snow covered plateau in southwestern Germany. The sky was overcast with altostratus clouds with a base altitude of 3 km. The apparent radiance of the snow surface as measured at an altitude of 6 km is roughly equal to the apparent radiance of the overcast sky. The minimum values of lower hemisphere radiance are associated with underlying areas of dark woods having an effective average reflectance of about .04 in this case. Notice that the effective reflectance of the snow covered areas is somewhat higher than the average value of 0.75 that was assumed for the model calculations.

The correspondence between the field measurements and the model calculations illustrated above are representative in general of the many such comparisons made during the course of model development and validation. It should be emphasized that the accuracy of the illustrated model calculations is enhanced considerably by the availability of the detailed vertical profile of scattering coefficient in the boundary layer, which is the major determinant of the fluctuations in path radiance in the troposphere. On the other hand, the correspondence between the actual and calculated radiance fields could be improved through relaxation of the constraint that other input variables be held equal to their typical or average values. For example, identification of an aerosol model appropriate for the boundary layer in a given synoptic situation would provide estimates of the single scattering phase function and single scattering albedo that are more realistic than the prescribed overall average values used in illustrated comparisons. A brief assessment of the sensitivity of estimates of the maximum detection range of distant objects to uncertainties in both atmospheric and target factors is given in the following Section.

6.0 SENSITIVITY OF TARGET DETECTION RANGE TO ENVIRONMENTAL AND TARGET FACTORS

Diagnostic calculations have been made routinely during the course of the investigations to determine the sensitivity of the model calculations to variations in the input data. In prior investigations (Hering, 1981), attention was directed primarily toward analysis of the sensitivity of contrast transmittance to changes or uncertainties in the relevant optical properties of the atmosphere. The interpretations of these results are straightforward in that, except for scintillation effects, Eq. 4 describes completely the atmospheric effects upon contrast transmittance. On the other hand, contrast transmittance must be coupled with the effects of specific target factors to estimate the maximum distance an object can be detected and identified. A given change in the slant-path, contrast transmittance may or may not be critical for target detection depending the minimum contrast required for detection. Thus, the assessment of the combined influences of atmospheric and target factors is important.

For this purpose, analytic techniques were introduced into the computer program to calculate visual detection range as an additional output variable. The representation of target information and visual search factors in this preliminary analysis are greatly simplified. Nevertheless, the results provide important insight into the sensitivity of visual detection distance to changes in specific atmospheric variables for selected combinations of target characteristics.

6.1 Determination of Visual Detection Range

The analytic representations of the contrast thresholds for visual detection were derived from basic visual data from the Tiffany experiments (Blackwell, 1946) and the Visibility Laboratory experiments (Taylor, 1964) which were adapted and summarized by Gordon (1979). The graphical representations of threshold contrast as a function of angular target size shown in Fig. 16 are taken

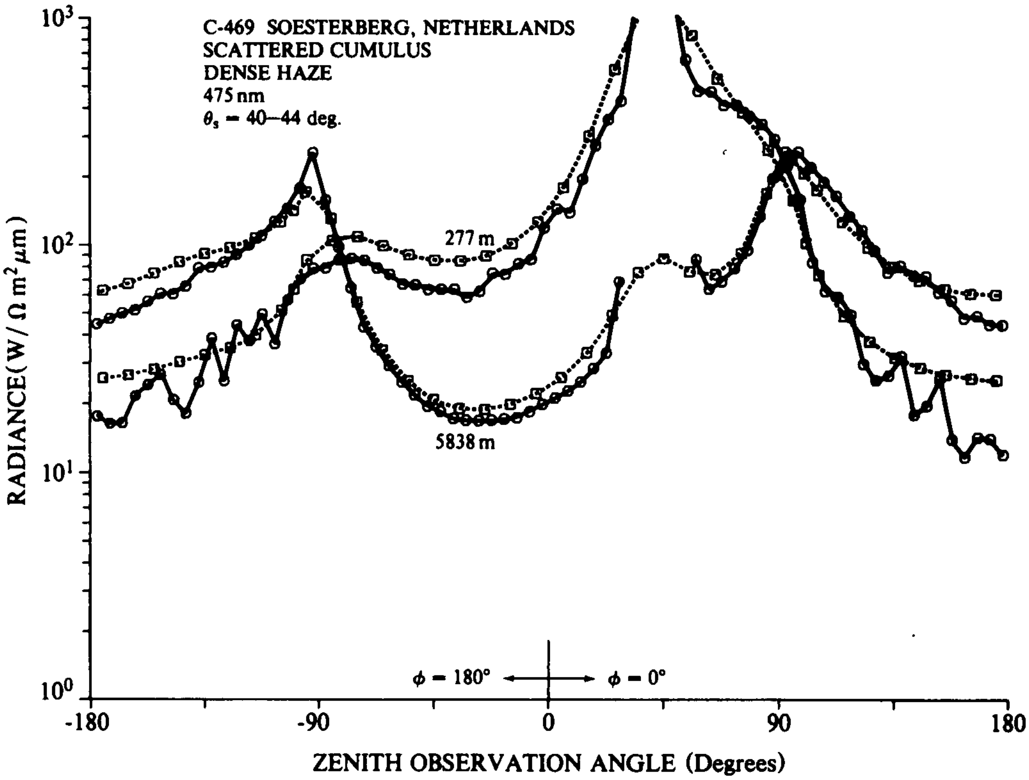

Fig. 10. Comparison of sky and terrain radiance as measured by airborne scanning radiometer (Johnson 1981d) (solid line) and model calculations (dashed line).

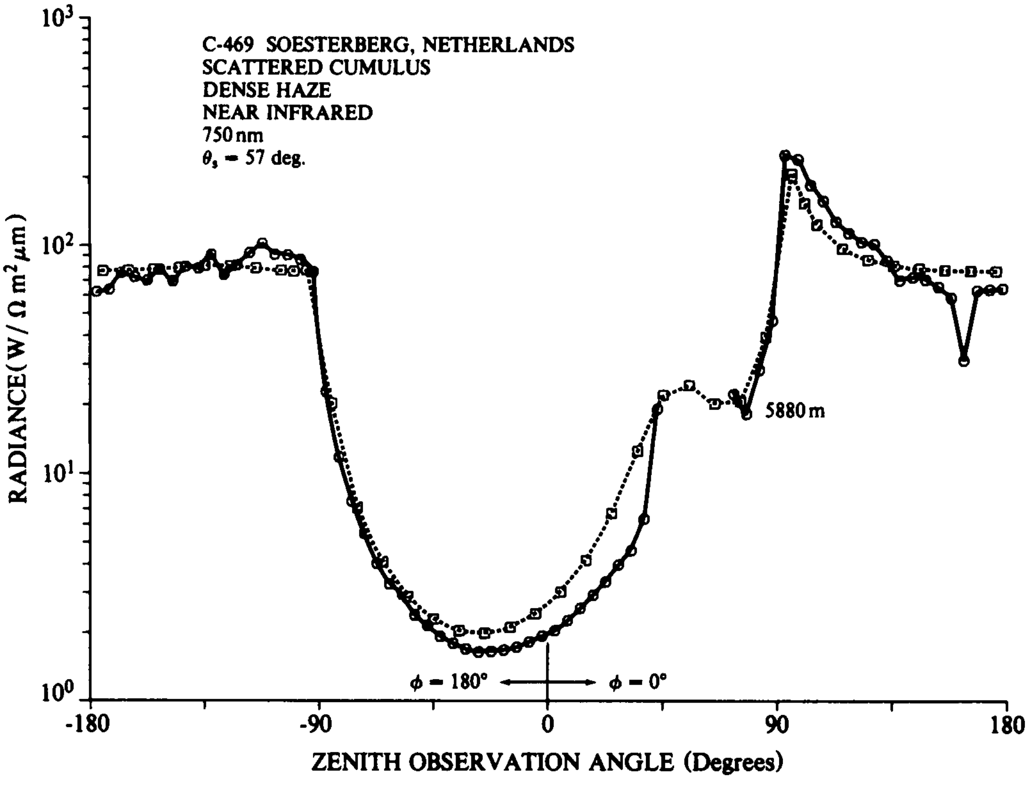

Fig. 11. Comparison of sky and terrain radiance as measured by airborne scanning radiometer (Johnson 1981d) (solid line) and model calculations (dashed line).

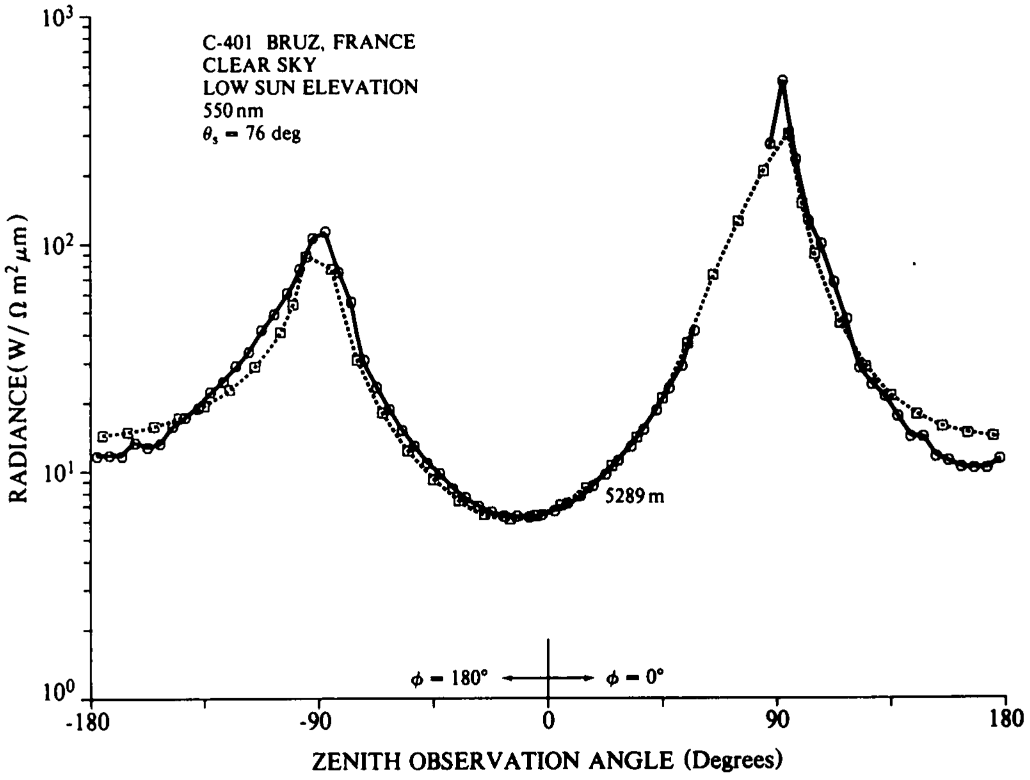

Fig. 12. Comparison of sky and terrain radiance as measured by airborne scanning radiometer (Johnson 1981d) (solid line) and model calculations (dashed line)

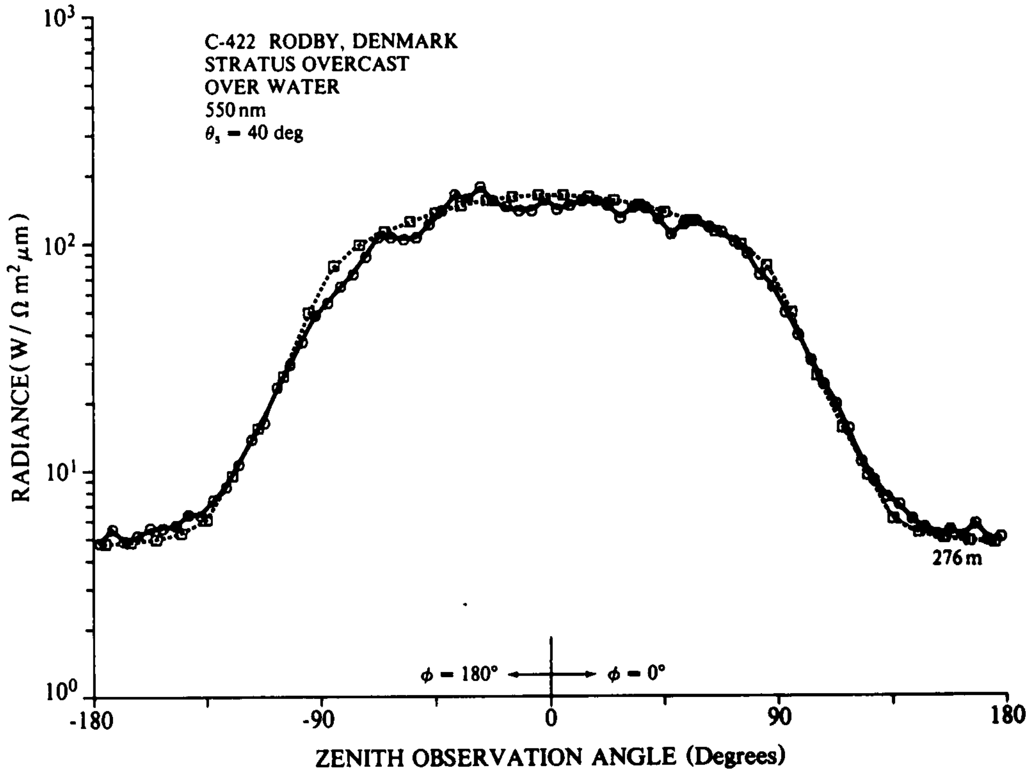

Fig. 13. Comparison of sky and terrain radiance as measured by airborne scanning radiometer (Johnson 1981d) (solid line) and model calculations (dashed line).

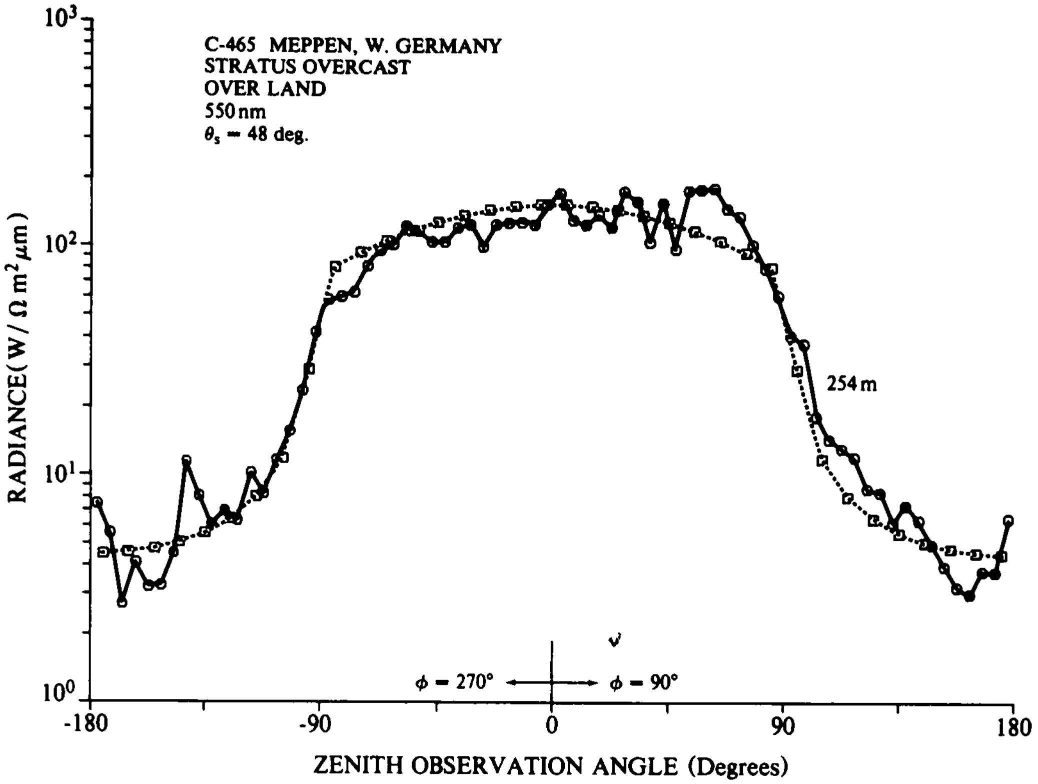

Fig. 14. Comparison of sky and terrain radiance as measured by airborne scanning radiometer (Johnson 1981d) (solid line) and model calculations (dashed line).

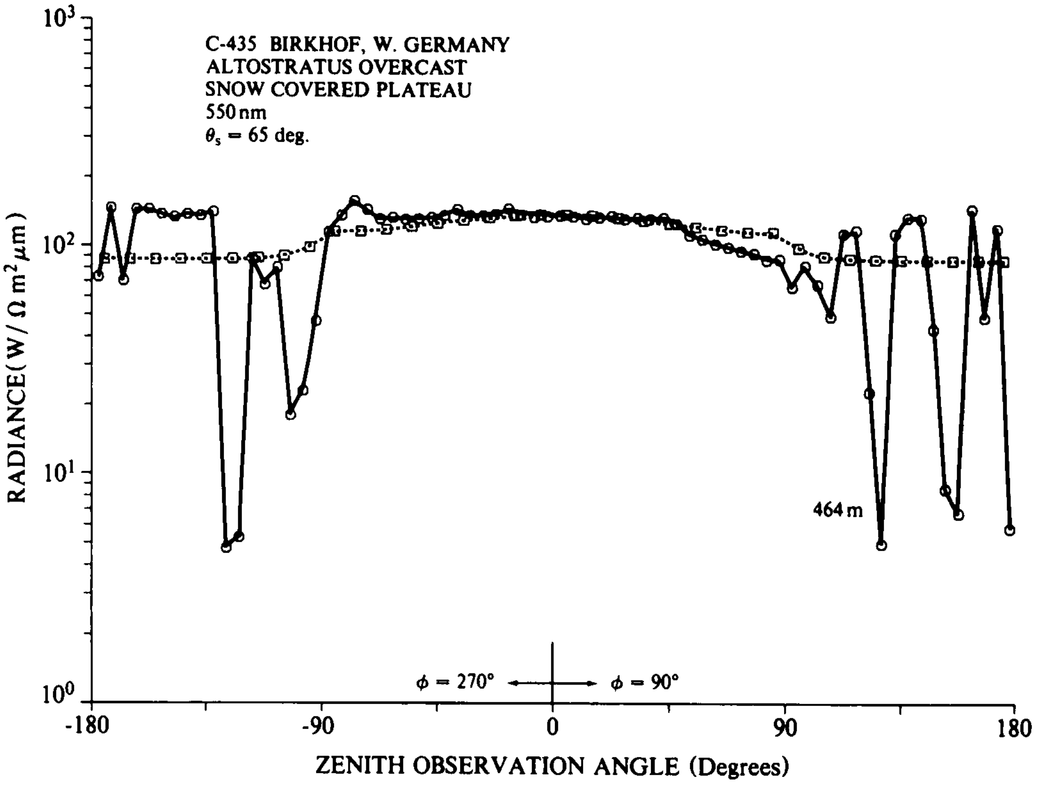

Fig. 15. Comparison of sky and terrain radiance as measured by airborne scanning radiometer (Johnson 1981d) (solid line) and model calculations (dashed line).

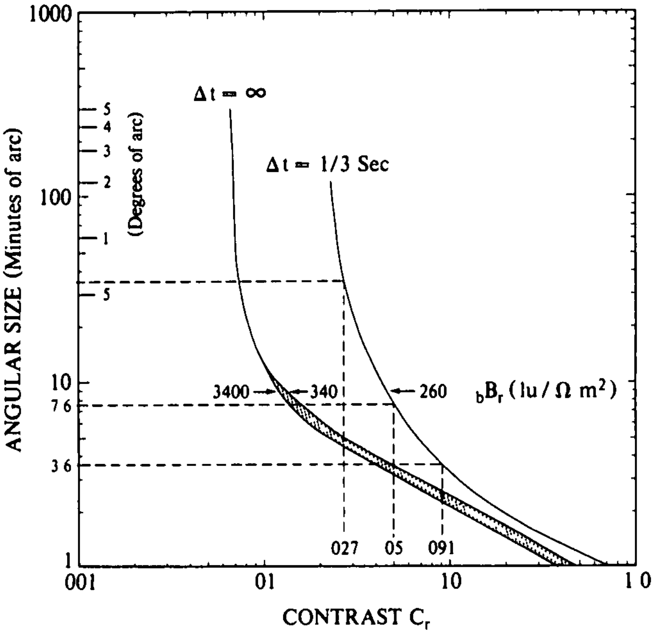

Fig. 16. Angular subtense of target as a function of threshold contrast for a 99 percent probability (confidence) of detection and a lack of knowledge of target position of ± 4 deg or more (Gordon, 1979). $_bB_r$ is the adaptation brightness and Δt is the assumed visual fixation (dwell) time.

directly from Fig. 1 of Gordon (1979). Two search modes are represented. The first corresponds to long duration viewing (>24 seconds, Tiffany data). The second corresponds to a viewing time of one-third of a second (Visibility Laboratory data), which is the approximate fixation time associated with search performed by the human eye (White, 1964).

From Fig. 16 we see that, for the normal range of daylight conditions, the visual contrast threshold does not vary significantly with background luminance. However, the contrast threshold does vary markedly with the angular subtense of the target. The relationships shown in Fig. 16, represent the contrast threshold associated with confident detection (99 percent probability) under conditions where the lack of knowledge of target position is ±4 degrees or more.

For application to the problem at hand, the prescribed relationships given in Fig. 16 were approximated analytically by the expression,

$$\ln \gamma = A+B(-\ln C_T) + C(-\ln C_T)^2 + D(-\ln C_T)^3 \quad (30)$$

where γ is the angular size of the target, C_T is the contrast detection threshold and A,B,C and D are the parameterization coefficients as determined for the two search modes.

Given the above method for the representation of target factors, let us now consider analytic representation of the model calculations of slant path contrast transmittance. The computational scheme provides discrete values of contrast transmittance for designated paths of sight. As an additional option, the contrast transmittance of air to ground observation paths for fixed values of azimuthal viewing angle and sensor altitude is represented through the method of least squares as a continuous function of path length (range) by the expression,

$$r = a+b[\ln \frac{C_r}{C_o}(z,\theta)] + c[\ln \frac{C_r}{C_o}(z,\theta)]^2 \quad (31)$$

Since the angular subtense of the target is less than a degree or so, the slant range, r, can be approximated by $r = d/\gamma$ where d is the effective diameter of the target. Given the inherent target contrast, C_o, the range associated with a selected value of apparent contrast C_r, is determined by Eq. 31. The maximum detection range for specified sensor altitude and azimuthal viewing angle corresponds to the range where $C_r = C_t$. The method of successive approximation yields rapidly converging solutions for maximum detection range from trial values of C_r and C_t using Eqs. 30 and 31.

6.2 Diagnostic Calculations of Visual Detection Distance

A series of additional model calculations were carried out to illustrate the relative sensitivity of target detection range to changes or uncertainties in some of the key variables. For this purpose, reference conditions were assumed which reflect a typical visual detection scenario for hazy atmospheres in the daytime. In an attempt to isolate the effects of fluctuations in individual factors, the procedure was to vary a given parameter over its normal range while holding all other reference conditions constant. The reference atmospheres used in this analysis are summarized in Appendix B (Ref. A for clear sky and Ref. B for overcast sky). The reference atmospheres have a surface equivalent visibility of 20 km and a boundary-layer hazy depth of 1 km. Except as noted, an ideal circular target is assumed having a diameter of 30m and an inherent contrast of one. The functional representation of psychophysical data of Taylor (1964) corresponding to the 0.33 sec fixation time (see Fig. 16) was used for the trial calculations except for the one comparative example (paragraph 6.2.5) based upon the Tiffany visual threshold data for a fixation time greater than 24 seconds.

Visual Horizontal Detection Distance versus Observer Altitude and Azimuthal Viewing Angle (Fig. 17).

For intermediate size targets of good inherent contrast, the maximum horizontal detection distance (ground range) increases significantly with increasing observer altitude in the lower troposphere above the boundary layer. The variations in ground range with azimuthal viewing angle are determined largely by the directional dependence of the path radiance as defined by the combined phase

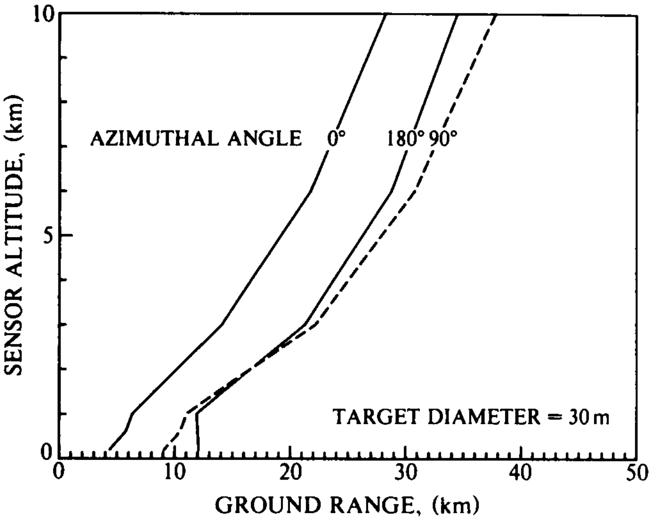

Fig. 17. Visual horizontal detection distance as a function of observer altitude and azimuthal observation angle.

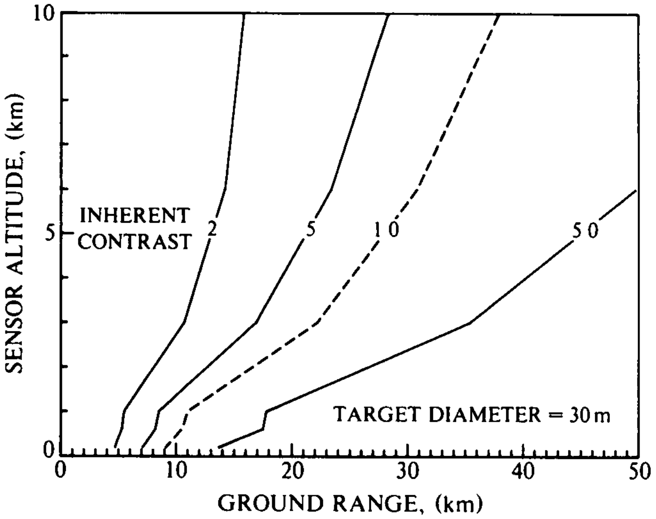

Fig. 18. Visual horizontal detection distance as a function of inherent contrast for 30-m target.

function for molecular and aerosol scattering. For the typical condition in the free atmosphere above the haze layer where the aerosol particles have low concentration, the difference in detection distance in the upsun ($\phi = 0$ deg) and downsun ($\phi = 180$ deg) viewing directions remains rather constant with increasing observer altitude above the boundary layer and increases with increasing solar zenith angle. Of special interest in Fig. 17 is the relatively small variation in detection range with azimuthal angle in the antisolar hemisphere as indicated by the rather close correspondence in the 180 degree (downsun) and 90 degree (cross sun) profiles. It should be noted that the trial calculations which follow in subsequent examples assume a 90-degree azimuthal viewing direction.

Visual Detection Distance versus Inherent Contrast (Fig. 18).

The rate of increase in visual detection range with increasing observer altitude depends significantly upon the initial target contrast. Notice in Fig. 18 the dramatic increase in detection range with increasing viewing altitude for bright targets viewed against a dark background ($C_o = 5$) as contrasted with the restricted increase in detection distance for low contrast targets ($C_o = 0.2$). As a point of reference information, the detection range is independent of the sign of the target contrast. For targets darker than the background, the lower contrast limit is $C_o = -1$ (black target). The inherent contrast of targets brighter than background is unbounded. The assumed reference value of target contrast of $C_o = 1$ (dashed curve) corresponds to the case where, under the same irradiance, the reflectivity of the target is twice the background reflectivity.

Visual Detection Distance versus Inherent Contrast for Reduced Target Size (Fig. 19).

Diagnostic model calculations for a smaller 5-m target diameter (Fig. 19) show the corresponding reduction

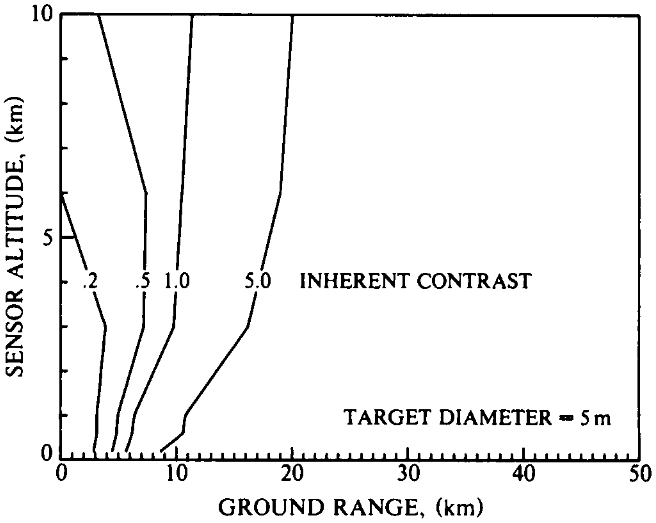

Fig. 19. Visual horizontal detection distance as a function of inherent contrast for 5-m target.

in visual detection distance as compared with the results for the 30-m target (Fig. 18). Notice, for example, in the case of a target of 0.2 inherent contrast under the assumed conditions, there is little advantage in increased detection range to be gained by climbing to an observation altitude above the haze layer top and that the reference target having 0.2 contrast cannot be detected with 99 percent probability above a viewing altitude of 6 km. The calculated visual detection range for 5-m targets for this example is everywhere less than 12 km for targets having an inherent contrast less than one.

Visual Detection Distance as a Function of Environmental Factors (Fig. 20).

Sensitivity calculations of the response of ground detection range to selected changes in individual factors

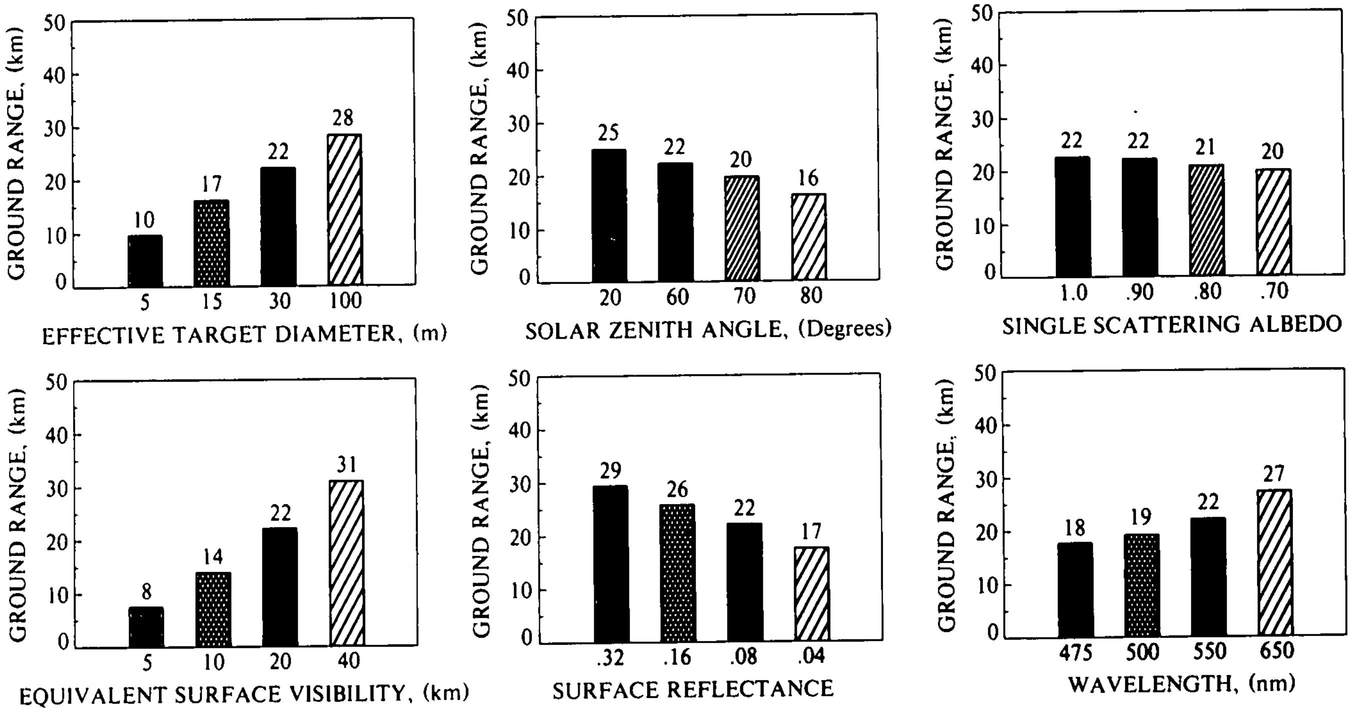

Fig. 20. Sensitivity of horizontal detection distance to changes in relevant factors. Solid bar in each case (22 km) corresponds to the calculation for reference target (30-m diameter) and reference atmosphere parameters. Surface target with a contrast of one is viewed against at a uniform background from an altitude of 3 km. For each case, all variables are fixed equal to reference values except for the variable under examination.

are shown in Fig. 20 for a ground target viewed from an altitude of 3 km. All variables except the factor under examination are held constant and equal to the reference values listed in paragraph 6.1 and Appendix B (Ref. A). The scattering and absorption coefficients are allowed to change only within the primary haze layer. The calculations assume a λ^{-1} wavelength dependence of the aerosol scattering coefficient and no changes in surface reflectance with wavelength. The illustrated changes in detection distance relative to changes in single scattering albedo were calculated assuming that the optical thickness of the haze layer remains constant, *i.e.* the scattering ratio was changed by an amount sufficient to compensate for the postulated change in absorption coefficient.

The solid bar in each of the graphs shown in Fig. 20 depicts the ground range (22 km) associated with the reference values for the individual variables. Notice for the prescribed conditions that a decrease in target distance of about 25 percent is associated with: (1) a reduction in target size by 50%; (2) a reduction in surface equivalent visibility by 35%; (3) an increase in solar zenith angle from 60 to 78 degrees; (4) a decrease in surface reflectance by 50 percent, and (5) a change in wavelength from 550 to 450 nm. The detection distance is less sensitive to changes in the absorption contribution to a fixed value of total volume extinction coefficient in the boundary layer. It should be emphasized that the results shown in Fig. 20 are specific only for the conditions assumed for the diagnostic calculations. Simultaneous changes in two or more variables could of course result in a much broader range in the variation of target detection distance.

Visual Detection Distance versus Visual Fixation Time (Fig. 21).

The variations in target detection distance that are associated with changes in stimulus duration are shown in Fig. 21. The two functional relationships for contrast threshold data used for the calculations are the same as those depicted in Fig. 16. As discussed above, the first applies to unlimited viewing time (>24 sec) and the second applies to the average fixation time (1/3 sec) for the performance of visual search by the human eye. Comparative calculations for the two viewing conditions are shown for two atmospheres. Both atmospheres and target factors are the same as reference conditions cited above except that the haze layer of depth 1.3 km is represented by the LOWTRAN (Shettle and Fenn, 1979) rural model atmosphere for relative humidity equal to 70 percent for the one case and for relative humidity equal to 99% in the other case. Notice that the relative difference in detection distance versus glimpse time for the example with high humidity and high extinction coefficient is roughly the same as that for the lower humidity and lower extinction coefficient example.

Visual Detection Distance for Overcast Sky (Fig. 22).

A cloudless atmosphere was assumed for the sensitivity analyses described above. Let us now consider

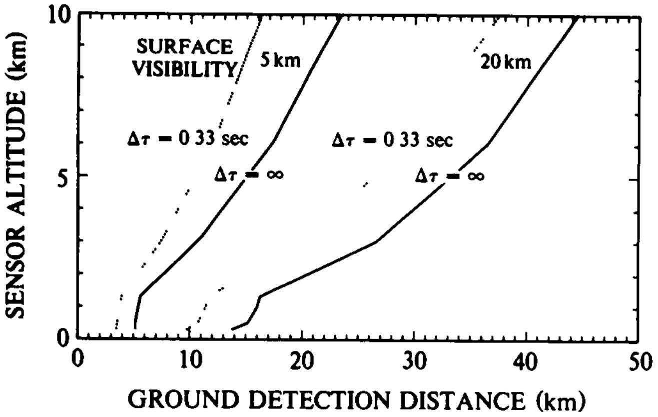

Fig. 21. Visual horizontal detection distance versus altitude for fixation times (Δt) of 0.33 sec and infinity. Calculations assume LOWTRAN rural model for boundary layer with 70 percent humidity (equivalent surface visibility of about 20 km) and with 99 percent humidity (equivalent surface visibility of about 5 km)

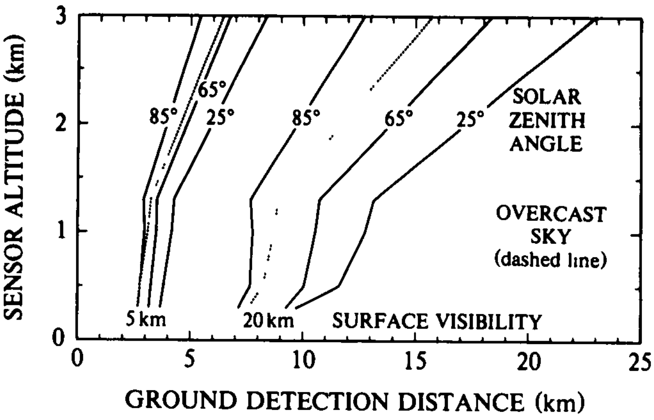

Fig. 22. Comparison of calculated target detection distance for a reference atmosphere with and without an overcast cloud layer. Calculations for clear sky case (solid lines) are shown for solar zenith angles of 25, 65, and 85 deg Calculations for case with stratocumulus overcast (dashed line) are for solar zenith angle of 55 deg.

briefly the behavior of contrast transmittance and the variations in target detection distance that are associated with overcast sky conditions. In the region below the cloud layer in the daytime, both the inherent background radiance $_bL_0(z_t,\theta,\phi)$ and the apparent radiance $_bL_r(z,\theta,\phi)$ are essentially proportional to the downwelling radiance at the cloud base when the direct sun component of the irradiance is small in comparison with the diffuse component. Thus, except for thin clouds with significant direct sun penetration, the contrast transmittance of slant paths below the cloud deck is to a good approximation independent of the downwelling irradiance from the cloud layer (see Eq. 4). However, the path radiance and radiance transmittance (hence the contrast transmittance) are of course strongly dependent upon the optical properties along the cloud free paths of sight below the overcast.

A comparison of target detection distance as calculated with and without an overcast cloud are shown in Fig. 22. The diagnostic calculations again were made using both the 70-percent and 99-percent humidity LOWTRAN rural models for the boundary layer. For the cloud free cases, calculations are shown for solar zenith angles of 25, 65 and 85 degrees. A solar zenith angle of 55 degrees and stratocumulus overcast of average optical depth were assumed for the calculation of the cloud case. As discussed above, the slant path contrast transmittance and detection distance for the overcast condition are not sensitive to cloud optical depth (or solar zenith angle). Notice in Fig. 22 that the calculated detection distance for the cloud case corresponds to the case where the cloud is removed and the solar zenith angle is near 75 degrees. This is a typical result for conditions where a Lambertian surface reflectance is assumed and the optical properties along the viewing path are the same for both the clear and cloud examples.

7.0 SUMMARY COMMENTS

The analytic techniques that were developed as part of the experimental optical measurement and analysis program provide relatively fast and consistent estimates of the visible spectrum contrast transmittance along vertically inclined paths of sight. Essential elements of the scheme include modeling techniques suitable for field use for the determination of the apparent background sky, cloud and terrain radiance distribution as well as the radiance transmittance along the viewing path. Emphasis was placed upon the development of algorithms which are simple and easy to apply yet are adaptable so as to take advantage of all relevant observations and forecast information. The procedures developed for the calculation of clear sky radiance distribution are directly applicable to the overcast sky condition through introduction of the appropriate optical properties of the cloud layer. Comparisons of model calculations with experimental aircraft measurements of cloud radiance indicate that use of average optical depths for various cloud types as derived from the SOLMET data base yields a good first approximation to the actual overcast cloud radiance distribution.

Another recent extension to the image transmission modeling procedures is the addition of techniques to deal with the combined influences of atmospheric and target factors in order to determine target detection range for objects located at the surface and viewed from aloft. Although the results described in this report pertain to simple targets with uniform backgrounds, the diagnostic model calculations provide insight into the relative importance of the uncertainties involved in the estimates of target detection distance. Not surprisingly, the determinations are most sensitive to uncertainties in the optical depth of the atmosphere which in turn impact directly all three components of contrast transmittance, *i.e.* the inherent and apparent background radiance and the path transmittance. The sensitivity calculations also confirm the strong dependence of target detection distance on knowledge of target and background reflectivity. The model capability for joint assessment of target and environmental effects on target detection range also reveals the interactive effects of such parameters as solar zenith angle, surface reflectivity, target size, and visual fixation time for overcast and clear sky conditions.

Efforts are underway to improve the methodology for estimating image transmission characteristics by relaxation of some of the constraints which limit the applicability and accuracy of the techniques. It is important in particular, to develop techniques to exploit expanding knowledge of the directional dependence of the reflectivity of various types of ground cover. Work is also underway to incorporate analytic techniques to estimate slant-path contrast transmittance and target detection distance for inclined paths of sight in fractional cloud cover conditions.

8.0 ACKNOWLEDGEMENTS

Technique development was made possible by the extensive base of information on the behavior of atmospheric optical properties created in recent years through the program of experimental measurement and analysis carried out by the Visibility Laboratory under the direction of Mr. Richard W. Johnson. The author is grateful to Mr. Eric P. Shettle of the Air Force Geophysics Laboratory, for his valuable suggestions and guidance, especially during the early phases of the investigation. He also expresses his appreciation to Ms. Jacqueline I. Gordon and Mr. Richard W. Johnson of the Visibility Laboratory and Lt.Col. John D. Mill of the Air Force Geophysics Laboratory for their many informative discussions during the course of this work and for suggestions on improvements in the modeling procedures. He wishes to thank Mr. Nils R. Persson and Ms. Miriam K. Oleinik for their expert assistance in the computer programming phases of this study.

9.0 REFERENCES

Barteneva, O.D., (1960) "Scattering Functions of Light in the Atmospheric Boundary Layer", Bull. Acad. Sci. U.S.S.R., Geophysics Series, 1237-1244.

Blackwell, H.R., (1946) "Contrast Thresholds of the Human Eye", J. Opt. Soc. Am. **36**, 624-643.

Cox, C. and W. Munk, (1954) "Measurements of the Roughness of the Sea Surface from Photographs of the Sun's Glitter", J. Opt. Soc. Am. **44**, 838-850.

Davies, R., (1980) "Fast Azimuthally Dependent Model of the Reflection of Solar Radiation by Plane-parallel Clouds", J. Appl. Opt. **19**, 250-255.

Duntley, S.Q., (1948) "Reduction of Contrast by the Atmosphere", J. Opt. Soc. Am. **38**, 179-191.

Duntley, S.Q., A.R. Boileau, and R.W. Preisendorfer, (1957) "Image Transmission by the Troposphere I", J. Opt. Soc. Am. **47**, 499-506.

Gordon, J.I., (1969a) "Directional Radiance (Luminance) of the Sea Surface", University of California, San Diego, Scripps Institution of Oceanography, Visibility Laboratory, SIO Ref. 69-20.

Gordon, J.I., (1969b) "Model for a Clear Atmosphere", J. Opt. Soc. Am. **59**, 14-18.

Gordon, J.I., (1979) "Daytime Visibility, A Conceptual Review", University of California, San Diego, Scripps Institution of Oceanography, Visibility Laboratory, SIO Ref. 80-1, AFGL-TR-79-0257, NTIS No. ADA 085 451.

Haurwitz, B., (1948) "Insolation in Relation to Cloud Type", J. Meteor. **5**, 110-113.

Hering, W.S., (1981) "An Operational Technique for Estimating Visible Spectrum Contrast Transmittance", University of California, San Diego, Scripps Institution of Oceanography, Visibility Laboratory, SIO Ref. 82-1, AFGL-TR-81-0198, ADA 111823.

Irvine, W.M., (1968) "Multiple Scattering by Large Particles II Optically Thick Layers", Astrophys. J. **152**, 823-834.

Johnson, R.W., (1981d) "Airborne Measurements of European Sky and Terrain Radiances", University of California, San Diego, Scripps Institution of Oceanography, Visibility Laboratory, SIO Ref. 82-2, AFGL-TR-81-0275.

Joseph, J.H., W.J. Wiscombe, and J.A. Weinman, (1976) "The delta-Eddington Approximation for Radiative Flux Transfer", Atmos. Sci. **33**, 2452-2459.

Lenoble, J., (1977) "Standard Procedures to Compute Radiation Transfer in a Scattering Atmosphere", Working Group Report, Radiation Commission, International Association of Meteorology and Atmospheric Physics, 125pp..

McKellar, B.H.J., and M.A. Box, (1981) "A Scaling Group of the Radiative Transfer Equation", J. Atmos. Sci., **38**, 1063-1068.

Shapiro, R., (1982) "Solar Radiative Flux Calculations from Standard Surface Meteorological Observations", Sci. Rpt. No. 1, Systems and Applied Sciences Corporation, AFGL-TR-82-0039, 53pp., AD 118775.

Shettle, E.P., and J.A. Weinman, (1970) "The Transfer of Solar Irradiance Through Inhomogeneous Turbid Atmospheres Evaluated by Eddington's Approximation", J. Atmos. Sci. **27**, 1048-1055.

Shettle, E.P., Private Communication. See Hering (1981), Appendix A.

SOLMET (1977), "Hourly Solar Radiation-Surface Meteorological Observations Vol. 1 - Users Manual. Vol. 2 Final Report, National Climatic Center, NOAA, EDIS, TD-9724 (1979).

Taylor, J.H., (1964) "The Use of Visual Performance Data in Visibility Prediction", Appl. Opt. **3**, 562-569.

Twomey, S., (1977) "Atmospheric Aerosols", Developments in Atmospheric Science 7, Elsevier Scientific Publishing Company, 245pp.

Welch, R.M., S.K. Cox, and W.G. Zdunkowski, (1980) "Calculations of the Variability of Ice Cloud Radiative Properties at Selected Solar Wavelengths", J. Appl. Opt., **19**, 3057-3066.

White, C.T., (1964) "Occular Behavior in Visual Search", Appl. Opt. **3**, 369-570.

APPENDIX A

SUMMARY OF INPUT DATA, COMPUTATION STEPS AND RESULTANT DATA

A.1 General Input Data

A.1.1 Number of atmospheric layers

A.1.2 Representative wavelength (μm)

A.1.3 Extraterrestrial solar (lunar) irradiance ($W/m^2\mu m$)

A.1.4 Rayleigh optical depth of top layer

A.1.5 Solar zenith angles (deg.)

A.1.6 Zenith viewing angles (deg.)

A.1.7 Average reflectance of underlying surface and reflectance of background in the vicinity of target if different than the average reflectance.

A.2 Input Data Each Layer

A.2.1 Base altitude (km)

A.2.2 Scattering mixing ratio

A.2.3 Single scattering albedo

A.2.4 Single scattering phase function (normalized to integral of one)

A.3 Computation Steps

A.3.1 Compute Rayleigh atmosphere optical thickness for each layer

A.3.2 Compute total optical thickness for each layer.

A.3.3 Compute optical depth for the base of each layer.

A.3.4 Compute single scattering phase function and asymmetry factors for each layer. (These parameters may be specified if desired in lieu of the use of model algorithms).

A.3.5 Transform optical depth, single scattering albedo, and asymmetry factor in accordance with delta-Eddington approximation.

A.3.6 Compute path function distribution for the base of each sub-layer (each layer is divided equally into 2 sub-layers).

A.3.7 Compute path radiance distribution for each sub-layer.

A.3.8 Compute path transmittance distribution for each sub-layer.

A.3.9 Compute sky/terrain radiance distribution at sub-layer boundaries.

A.3.10 Compute slant path contrast transmittance of selected paths.

A.4 Output Tables and Data

A.4.1 Path radiance, $L_r(z,\theta,\beta)$, for $0° \leqslant \theta \leqslant 85°$ (upward looking paths) for selected levels (max 5) for each θ_s (i.e. Sky Radiance) ($W/m^2\mu m\ sr$)

A.4.2 Path radiance, $L_r(z,\theta,\beta)$ for $95° \leqslant \theta \leqslant 180°$ (downward looking paths) for selected levels (max 5) for each θ_s ($W/m^2\mu m\ sr$)

A.4.3 Path plus terrain radiance $L_r(z,\theta,\beta)$ for $95° \leqslant \theta \leqslant 180°$ for selected levels (max 5) for each θ_s ($W/m^2\mu m\ sr$)

A.4.4 Contrast transmittance, $T_c(z,\theta,\beta)$ between object and sensor altitudes (max. 5 altitude intervals) for $0° \leqslant \theta \leqslant 85°$ and for each θ_s.

A.4.5 Contrast transmittance $T_c(z,\theta,\beta)$ between object and sensor altitudes (max. 5) for $95° \leqslant \theta \leqslant 180°$ and for each θ_s.

A.5 Additional Output From The Supplemental Eddington Computer Program

The standard Eddington computer program is employed as an integrated part of the model calculations of contrast transmittance. The following output from the program as modified by the delta-Eddington transformation of input parameters is available in tabular form for the base of each sub-layer and for each solar zenith angle:

- optical depths, τ and τ'
- components of Eddington diffuse radiance, $L_D(z)$ and $L_{D'}(z)$ ($W/m^2\mu m\ sr$)
- total scalar irradiance ($W/m^2\mu m$)
- downward diffuse irradiance ($W/m^2\mu m$)
- upward diffuse irradiance ($W/m^2\mu m$)
- solar irradiance ($W/m^2\mu m$)
- total downward irradiance ($W/m^2\mu m$)

SPECIFIC INPUT DATA FOR MODEL CALCULATIONS

Figure Number	8	9	10	11	12	13	14	15	Ref A	Ref B
Flight Number	379	466	469	469	401	422	465	435	-	-
Wavelength (nm)	475	475	475	750	550	475	550	550	550	-
Primary Haze Layer										
Upper Altitude Limit (km)	1 6	1 3	1 2	1 2	1 0	1 8	1 6	3 0	1 0	1 0
Scattering Ratio	5 1	12 0	28 0	54 0	5 3	25 0	9 0	9 3	13 0	1 3
Single Scattering Albedo	93	87	87	87	97	90	90	90	90	90
Upper Troposphere										
Scattering Ratio	1 16	1 16	1 16	1 5	1 2	1 2	1 16	1 2	1 2	1 2
Single Scattering Albedo	99	99	99	99	99	99	99	99	99	99
Cloud Layer										
Optical Depth						22 0	22 0	15 9		22 0
Base Altitude (km)						1 8	1 6	3 0		1 0
Single Scattering Albedo						1 0	1 0	1 0		1 0
Solar Zenith Angle (Deg)	36	41	44	48	72	40	51	63	60	60
Surface Reflectance	Frsnl	06	06	30	06	Frsnl	06	75	08	08

APPENDIX C

GLOSSARY AND NOTATION

The notation used in reports and journal articles produced by the Visibility Laboratory staff follows, in general, the rules set forth in pages 499 and 500, Duntley *et al.* (1957). These rules are:

- Each optical property is indicated by a basic (parent) symbol.
- A presubscript may be used with the parent symbol as an identifier, *e.g.*, b indicates background while t denotes an object, *i.e.* target.
- A postsubscript may be used to indicate the length of a path of sight, *e.g.*, r denotes an apparent property as measured at the end of a path of sight of length r, while o denotes an inherent property based on the hypothetical concept of a photometer located at zero distance from an object, *i.e.* target.
- A postsuperscript* or postsubscript$_{*}$, is employed as a mnemonic symbol signifying that the radiometric quantity has been generated within the path or path segment by the scattering of ambient light reaching the path from all directions and/or by emission.
- The parenthetical attachments to the parent symbol denote altitude and direction. The letter z indicates altitude in general; z_t is used to specify the altitude of a target. The direction of a path of sight is specified by the zenith angle θ and the azimuth ϕ. In the case of irradiances, the downwelling irradiance is designated by d, the upwelling by u.
- The radiometric symbols used herein now correspond to the OSA recommendations in Section 1 of Driscoll and Vaughn (1978). Prior to June 1980, the symbol used for radiance L was N, for irradiance E was H, and for attenuation length $\mathcal{L}$ was L.

Symbol	Units	Quantity
$A(z)$	none	Albedo at altitude z, defined $A(z) = E(z,u) \,/\, E(z,d)$.
$a(z)$	m^{-1}	Absorption coefficient.
$C(z)$	$sr^{-1}\ m^{-1}$	Diffuse component of the solar almucantar sky radiance ratio to the sun scalar irradiance and relative airmass $C(z) = \int_{4\pi} L(z,\theta',\phi')\sigma(z,\beta')d\Omega \,/\, {}_s\epsilon(z) + L_{*_a}(z) \,/\, {}_s\epsilon(z)$.
c	m/s	Speed of light $c = 2.99792458E8$.
c_1	Wm^2	First radiation constant $c_1 = 2\pi hc^2 = 3.741832E{-16}$.
c_2	mK	Second radiation constant $c_2 = ch/k = 1.438786E{-2}$.
$D(z)$	none	Radiance distribution function $D(z) = \int_{4\pi} L(z,\theta',\phi') sec\theta' d\Omega \,/\, \epsilon(z)$.
$D(\lambda)$	none	Limb darkening factor relating the average sun radiance and the center sun radiance $D(\lambda) = {}_s\bar{L}_o \,/\, {}_sL_o$.
E_λ	W/m^2	Spectral irradiance (formerly symbol H) defined as $E_\lambda = \int_{2\pi} L_\lambda(z,\theta,\phi) \cos\theta \, d\Omega$.

Symbol	Units	Quantity
E	$W/m^2 \mu m$	Broad band sensor irradiance, defined as $E = \int_0^\infty E_\lambda \overline{S_\lambda T_\lambda}\, d\lambda \,/\, \delta\lambda$.
$E(z,d)$	W/m^2	Irradiance produced by downwelling flux as determined on a horizontal flat plate at altitude z [formerly $H(z,d)$]. In this report d is used in place of the minus sign in the notation $[H(z,-)]$ which appears in Duntley (1969). This property may be defined by the equation $E(z,d) = \int_{2\pi} L(z,\theta',\phi') \cos\theta' \, d\Omega'$.
$E(z,u)$	W/m^2	Irradiance produced by the upwelling flux as determined on a horizontal flat plane at altitude z [formerly $H(z,u)$]. Here u is substituted for the plus sign formerly used in the notation $[H(z,+)]$.
$H(z)$	m	Scale height at altitude z, the height of a homogeneous atmosphere having the density of the layer at altitude z.
h	J/s	Planck constant $h = 6.626176E{-}34$.
k	J/K	Boltzmann constant $k = 1.380662E{-}23$.
L_λ	$W/sr\ m^2$	Spectral radiance (former symbol N).
L	$W/sr\ m^2 \mu m$	Broad band sensor radiance is defined as $L = \int_0^\infty L_\lambda \overline{S_\lambda T_\lambda}\, d\lambda \,/\, \delta\lambda$.
$L_o(z_t,\theta,\phi)$	$W/sr\ m^2$	Inherent radiance based on the hypothetical concept of a photometer located at zero distance from an object at altitude z in the direction specified by zenith angle θ and azimuth ϕ.
$L_r(z,\theta,\phi)$	$W/sr\ m^2$	Apparent radiance as determined at altitude z, from the end of a path of sight of length r at zenith angle θ and azimuth ϕ. This property may be defined by $L_r(z,\theta,\phi) = L_o(z_t,\theta,\phi)\, T_r(z,\theta) + L_r^*(z,\theta,\phi)$.
$L(\lambda,T)$	$W/sr\ m^2$	Black body radiance at wavelength λ and temperature T.
$L_q(z,\theta,\phi)$	$W/sr\ m^2$	Equilibrium radiance at altitude z with the direction of the path of sight specified by zenith angle θ and azimuth ϕ. This property is a point function of position and direction. As discussed by Duntley *et al.* (1957), many image transmission phenomena are most clearly understood in terms of the concept of equilibrium radiance. This concept is a natural consequence of the equation of transfer which states analytically that in any path segment the difference between the output and input radiances is attributable to a gain term and a loss term, such that some unique equilibrium radiance $L_q(z,\theta,\phi)$ must exist at each point such that the loss of radiance within the path segment is exactly balanced by the gain, *i.e.*, $\Delta L(z,\theta,\phi) = 0$.

APPENDIX C

Symbol	Units	Quantity
		By virtue of this concept and the equation of transfer, one can show that each segment of every path of sight has associated with it an equilibrium radiance, and that the space rate of change in image forming radiance caused by the path segment is in such a direction as to cause the output radiance to be closer to the equilibrium radiance than is the input radiance. This segment by segment convergence of the apparent radiance of the object field to the dynamic equilibrium radiance was clearly illustrated by the data in the 1957 paper referenced above.
$L_*(z,\theta,\phi)$	$W/sr\ m^2$	Path function at altitude z with the direction of the path of sight specified by zenith angle θ and azimuth ϕ. This property is defined by the equation $L_*(z,\theta,\phi) = L_{*_s}(z,\theta,\phi) + L_{*_a}(z)$.
$L_{*_s}(z,\theta,\phi)$	$W/sr\ m^2$	Path function due to scattering, defined by $L_*(z,\theta,\phi) = \int_{4\pi} \sigma(z,\beta')L(z,\theta',\phi')d\Omega'$.
$L_{*_a}(z)$	$W/sr\ m^2$	Path function due to emittance (absorption) $L_{*_a}(z) = a(z)\ L(\lambda,T)$.
$L_r^*(z,\theta,\phi)$	$W/sr\ m^2$	Path radiance as determined at altitude z at the end of a path of sight of length r in the direction of zenith angle θ and azimuth ϕ.
$L_\infty^*(z,\theta,\phi)$	$W/sr\ m^2$	Sky radiance at altitude z, zenith angle θ and azimuth ϕ. Also the path radiance for the path of sight of length ∞ from out of the atmosphere to altitude z.
${}_sL_\infty(z,\theta_s,\phi)$	$W/sr\ m^2$	Apparent radiance of the center of the solar disk as determined from the end of a path of sight of length ∞ from out of the atmosphere to altitude z at the zenith angle of the sun θ_s.
$\mathcal{L}(z)$	m	Attenuation length at altitude z. The attenuation length is the distance at which the signal is attenuated to 1/e.
$M(\lambda,T)$	W/m^2	Black body exitance (emittance) $M(\lambda,T) = \pi L(\lambda,T)$.
$m(\lambda,T)$	W/m^2	Black body scalar exitance (emittance) $m(\lambda,T) = 4\pi L(\lambda,T)$.
$m_*(z)$	W/m^3	Scalar exitance (emittance) per length $m_*(z) = \int_{4\pi} L_*(z,\theta,\phi)d\Omega$.
$m_{*_s}(z)$	W/m^3	Scalar exitance (emittance) per length due to scattering $m_{*_s}(z) = \int_{4\pi} L_{*_s}(z,\theta,\phi)d\Omega = \epsilon(z)s(z)$.
$m_{*_a}(z)$	W/m^3	Scalar exitance (emittance) per length due to absorption $m_{*_a}(z) = a(z)m(\lambda,T)$.
$m_\infty(z,\theta)$	kg/m^2	Absolute air mass at angle θ $m_\infty(z,\theta) = \int_z^\infty \rho(z)dr$.

Symbol	Units	Quantity
$m_\infty(z,\theta)/m_\infty(z,0^\circ)$	none	Relative optical air mass.
$m(\theta_s)$	none	Relative optical airmass at zenith angle of the sun, shorthand for $m_\infty(z,\theta_s)/m_\infty(z,0^\circ)$.
$N(z)$	none	Refractive modulus $N(z) = [n(z) - 1]E6$.
$n(z)$	none	Refractive index.
$Q(z)$	none	Optical scattering mixing ratio at altitude z. This quantity is defined as the ratio of the total volume scattering coefficient at altitude z, to the molecular (or Rayleigh) volume scattering coefficient at the same altitude z. $Q(z) = s(z)/{}_R s(z)$.
$\mathcal{Q}(z,\beta)$	none	Volume scattering function ratio at altitude z. This quantity is defined as the ratio of the total volume scattering function at altitude z and scattering angle β, to the molecular (or Rayleigh) volume scattering function at the same altitude and scattering angle. $\mathcal{Q}(z,\beta) = \sigma(z,\beta) \,/\, {}_R\sigma(z,\beta)$.
r	m	Path length, for paths of sight at zenith angles 0 to 70 degrees, $r = sec\theta \, \Delta z$.
$\overline{S_\lambda T_\lambda}$	none	Standardized relative spectral response of filter/cathode combination where S_λ is spectral sensitivity of the multiplier phototube cathode and T_λ is spectral transmittance of optical filter. The relative spectral response values are normalized to the peak value.
$s(z)$	m^{-1}	Total volume scattering coefficient as determined at altitude z. This property may be defined by the equations $s(z) = \int_{4\pi} \sigma(z,\beta)\,d\Omega = {}_R s(z) + {}_M s(z).$ In the absence of atmospheric absorption, the total volume scattering coefficient is numerically equal to the attenuation coefficient.
${}_M s(z)$	m^{-1}	Volume scattering coefficient for Mie *i.e.* particulate or droplet, scattering at altitude z.
${}_R s(z)$	m^{-1}	Volume scattering coefficient for Rayleigh *i.e.* molecular, scattering at altitude z.
T	K	Absolute temperature in degrees Kelvin.
$T_r(z,\theta)$	none	Radiance transmittance as determined at altitude z for a path of sight of length r at zenith angle θ (formerly referred to as "beam" transmittance). This property is independent of azimuth in atmospheres having horizontal uniformity. It is always the same for the designated path of sight or its reciprocal.
$T_\infty(z,\theta)$	none	Radiance transmitance for the path of sight at zenith angle θ from out of the atmosphere to the altitude z.

APPENDIX C

Symbol	Units	Quantity
$t_{\Delta z}(z)$	none	Optical thickness $t_{\Delta z}(z) = \int_{z_t}^{z} \alpha(z)dz$.
${}_a t_{\Delta z}(z)$	none	Absorption optical thickness ${}_a t_{\Delta z}(z) = \int_{z_t}^{z} a(z)dz$.
${}_M t_{\Delta z}(z)$	none	Mie optical thickness ${}_M t_{\Delta z}(z) = \int_{z_t}^{z} {}_M s(z)dz$.
${}_R t_{\Delta z}(z)$	none	Rayleigh or molecular optical thickness ${}_R t_{\Delta z}(z) = \int_{z_t}^{z} {}_R s(z)dz$.
w	J/m^3	Radiant density.
W	W	Watt W = J/s.
z	m	Altitude, usually used as above ground level.
z_t	m	Altitude of any applicable object or target.
$\alpha(z)$	m^{-1}	Volume attenuation coefficient as determined at altitude z. $\alpha(z) = a(z) + s(z)$.
β	deg	Symbol for scattering angle of flux from a light source. It is equal to the angle between the line from the source to any unit scattering volume and the path of a ray scattered off this direct line. See illustration. 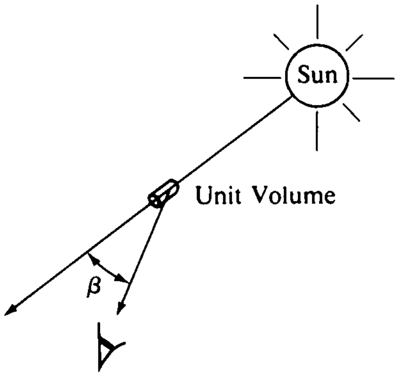
Δ	none	Symbol to indicate incremental quantity and used with r and z to indicate small, discrete increments in path length r and altitude z.
$\delta\lambda$	nm	Effective passband (formerly designated "response area") for a filtered sensor is defined as $\delta\lambda = \int_0^\infty \overline{S_\lambda T_\lambda}\, d\lambda$.

Symbol	Units	Quantity
$\epsilon(z)$	W/m^2	Scalar irradiance. This may be defined as the radiant flux arriving at a point, from all directions about that point, at altitude z (Tyler and Preisendorfer (1962)). $\epsilon(z) = \int_{4\pi} L(z,\theta',\phi')\,d\Omega'$.
${}_d\epsilon(z)$	W/m^2	Diffuse scalar irradiance ${}_d\epsilon(z) = \epsilon(z) - {}_s\epsilon(z)$.
${}_s\epsilon(z)$	W/m^2	Sun scalar irradiance at altitude z ${}_s\epsilon(z) = {}_s\epsilon(\infty)\,T_\infty(z,\theta_s)$.
ζ	m	Radius of the earth.
θ	deg	Symbol for zenith angle. This symbol is usually used as one of two coordinates to specify the direction of a path of sight.
θ'	deg	Symbol for zenith angle usually used as one of two coordinates to specify the direction of a discrete portion of the sky.
θ_s	deg	Zenith angle of the sun.
λ	nm	Symbol for wavelength.
$\bar{\lambda}$	nm	Mean wavelength is defined as $\bar{\lambda} = \int_0^\infty \lambda\, \overline{S_\lambda T_\lambda}\, d\lambda \,/\, \delta\lambda$.
$\mu(z,\beta)$	sr^{-1}	Ratio of solar almucantar sky radiance to scalar sun irradiance and airmass. $\mu(z,\beta) = L^{\bullet}_{\infty}(z,\theta_s,\beta) \,/\, [\,{}_s\epsilon(z)\,m(\theta_s)]$.
$\xi(z)$	W/m^2	Net irradiance. $\xi(z) = E(z,d) - E(z,u)$.
$\rho(z)$	kg/m^3	Density at altitude z.
$\sigma(z,\beta)$	$m^{-1}sr^{-1}$	Symbol for volume scattering function. Parenthetical symbols are z to designate altitude and β to designate the scattering angle from a source.
$\sigma(z,\beta)/s(z)$	sr^{-1}	Normalized volume scattering function. This may be defined by the equation $\int_{4\pi} [\,\sigma(z,\beta) \,/\, s(z)]\,d\Omega = 1$.
$\tau_{\Delta z}(z,\beta)$	sr	Optical thickness function. $\tau_{\Delta z}(z,\beta) = \int_{z_t}^{z} \sigma(z,\beta)\,dz$.

APPENDIX C

Symbol	Units	Quantity
ϕ	deg	Symbol for azimuth. The azimuth is the angle in the horizontal plane of the observer between a fixed point and the path of sight. The fixed point may be for example, true North, the bearing of the sun, or the bearing of the moon. This symbol is usually used as one of two coordinates to specify the direction of a path of sight.
ϕ'	deg	This symbol for azimuth is usually used as one of two coordinates to specify the direction of a discrete portion of the sky.
ψ	deg	Angular solar radius at true earth-to-sun distance.
$\bar{\psi}$	deg	Angular solar radius at mean solar distance.
Ω	*sr*	Symbol for solid angle. For a hemisphere, $\Omega = 2\pi$ steradians. For a sphere, $\Omega = 4\pi$ steradians.
$\omega(z)$	none	Single scattering albedo $\omega(z) = s(z) / \alpha(z)$.

APPENDIX C

Table C.1. Notational equivalencies

Chandrasekhar (1960)		Visibility Laboratory	
Symbol	Definition	Symbol	Definition
E	Radiant energy	E	Irradiance
πF	Net flux	ξ	Net irradiance
I	Specific intensity	$L(z,\theta,\phi)$	Radiance
J	Average intensity	$\epsilon/4\pi$	Average radiance
j	Mass emission coefficient	$\dfrac{L_*(z,\theta,\phi)}{\rho(z)}$	Path function/density
$j\rho$	Mass emission coefficient × density	$L_*(z,\theta,\phi)$	Path function
$j^{(s)}$	Mass emission coefficient due to scattering	$\dfrac{L_{*_s}(z,\theta,\phi)}{\rho(z)}$	Path function due to scattering divided by the density
k	Mass absorption coefficient	α/ρ	Attenuation coefficient divided by the density
$k\rho$	Mass absorption coefficient × density	$\alpha(z)$	Attenuation coefficient
$p(\cos\Theta)$	Phase function	$4\pi\sigma(\beta)/\alpha$	Four π times volume scattering function/attenuation coefficient
s	Thickness	r	Path length
$\mathfrak{J}$	Source function	L_q	Equilibrium radiance
u	Integrated energy density	w	Radiant density
ω_o	Single scattering albedo	$\omega(z)$	Single scattering albedo
Θ	Scattering angle	β	Scattering angle
ϑ	Polar angle	θ	Zenith angle
μ	cosine of polar angle	$\cos\theta$	cosine of zenith angle
ν	Frequency	$1/\lambda$	Inverse wavelength
ρ	Density	ρ	Density
τ	Normal optical thickness	$t_{\Delta z}$	Optical thickness
φ	Azimuth	ϕ	Azimuth
ω	Solid angle	Ω	Solid angle

APPENDIX D

VISIBILITY LABORATORY CONTRACTS AND RELATED PUBLICATIONS

Previous Related Contracts:
F19628-73-C-0013, F19628-76-C-0004

PUBLICATIONS:

Duntley, S.Q., R.W. Johnson, J.I. Gordon, and A. R. Boileau, "Airborne Measurements of Optical Atmospheric Properties at Night", University of California, San Diego, Scripps Institution of Oceanography, Visibility Laboratory, SIO Ref. 70-7, AFCRL-70-0137, NTIS No. AD 870 734 (1970).

Duntley, S.Q., R.W. Johnson, and J.I. Gordon, "Airborne Measurements of Optical Atmospheric Properties in Southern Germany", University of California, San Diego, Scripps Institution of Oceanography, Visibility Laboratory, SIO Ref. 72-64, AFCRL-72-0255, NTIS No. AD 747 490 (1972a).

Duntley, S.Q., R.W. Johnson, and J.I. Gordon, "Airborne and Ground-Based Measurements of Optical Atmospheric Properties in Central New Mexico", University of California, San Diego, Scripps Institution of Oceanography, Visibility Laboratory, SIO Ref. 72-71, AFCRL-72-0461, NTIS No. AD 751 936 (1972b).

Duntley, S.Q., R.W. Johnson, and J.I. Gordon, "Airborne Measurements of Optical Atmospheric Properties, Summary and Review", University of California, San Diego, Scripps Institution of Oceanography, Visibility Laboratory, SIO Ref. 72-82, AFCRL-72-0593, NTIS No. AD 754 898 (1972c).

Duntley, S.Q., R.W. Johnson, and J.I. Gordon, "Airborne Measurements of Optical Atmospheric Properties in Southern Illinois", University of California, San Diego, Scripps Institution of Oceanography, Visibility Laboratory, SIO Ref. 73-24, AFCRL-TR-73-0422, NTIS No. AD 774 597 (1973).

Duntley, S.Q., R.W. Johnson, and J.I. Gordon, "Airborne and Ground-Based Measurements of Optical Atmospheric Properties in Southern Illinois", University of California, San Diego, Scripps Institution of Oceanography, Visibility Laboratory, SIO Ref. 74-25, AFCRL-TR-74-0298, NTIS No. ADA 013 164 (1974).

Duntley, S.Q., R.W. Johnson, and J.I. Gordon, "Airborne Measurements of Optical Atmospheric Properties in Western Washington", University of California, San Diego, Scripps Institution of Oceanography, Visibility Laboratory, SIO Ref. 75-24, AFCRL-TR-75-0414, NTIS No. ADA 026 036 (1975a).

Duntley, S.Q., R.W. Johnson, and J.I. Gordon, "Airborne Measurements of Optical Atmospheric Properties, Summary and Review II", University of California, San Diego, Scripps Institution of Oceanography, Visibility Laboratory, SIO Ref. 75-26, AFCRL-TR-75-0457, NTIS No. ADA 022 675 (1975b).

Duntley, S.Q., R.W. Johnson, and J.I. Gordon, "Airborne Measurements of Optical Atmospheric Properties in Northern Germany", University of California, San Diego, Scripps Institution of Oceanography, Visibility Laboratory, SIO Ref. 76-17, AFGL-TR-76-0188, NTIS No. ADA 035 571 (1976).

Duntley, S.Q., R.W. Johnson, and J.I. Gordon, "Airborne Measurements of Atmospheric Volume Scattering Coefficients in Northern Europe, Spring 1976", University of California, San Diego, Scripps Institution of Oceanography, Visibility Laboratory, SIO Ref. 77-8, AFGL-TR-77-0078, NTIS No. ADA 046 290 (1977).

Duntley, S.Q., R.W. Johnson, and J.I. Gordon, "Airborne Measurements of Atmospheric Volume Scattering Coefficients in Northern Europe, Fall 1976", University of California, San Diego, Scripps Institution of Oceanography, Visibility Laboratory, SIO Ref. 78-3, AFGL-TR-77-0239, NTIS No. ADA 057 144 (1978a).

Duntley, S.Q., R.W. Johnson, and J.I. Gordon, "Airborne Measurements of Atmospheric Volume Scattering Coefficients in Northern Europe, Summer 1977", University of California, San Diego, Scripps Institution of Oceanography, Visibility Laboratory, SIO Ref. 78-28, AFGL-TR-78-0168, NTIS No. ADA 068 611 (1978b).

Duntley, S.Q., R.W. Johnson, and J.I. Gordon, "Airborne Measurements of Optical Atmospheric Properties, Summary and Review III", University of California, San Diego, Scripps Institution of Oceanography, Visibility Laboratory, SIO Ref. 79-5, AFGL-TR-78-0286, NTIS No. ADA 073 121 (1978c).

Fitch, B.W. and T.S. Cress, "Measurements of Aerosol Size Distribution in the Lower Troposphere over Northern Europe", J. Appl. Met. **20**, No. 10, 1119-1128, also University of California, San Diego, Scripps Institution of Oceanography, Visibility Laboratory, SIO Ref. 81-18, AFGL-TR-80-0192, NTIS No. ADA 104 272 (1981).

Gordon, J.I., C. F. Edgerton, and S.Q. Duntley, "Signal-Light Nomogram", J. Opt. Soc. Am. **65**, 111-118 (1975).

Gordon, J.I., J. L. Harris, Sr., and S.Q. Duntley, "Measuring Earth-to-Space Contrast Transmittance from Ground Stations", Appl. Opt. **12**, 1317-1324 (1973).

Gordon, J.I., "Model for a Clear Atmosphere", J. Opt. Soc. Am. **59**, 14-18 (1969).

Gordon, J.I., "Daytime Visibility, A Conceptual Review", University of California, San Diego, Scripps Institution of Oceanography, Visibility Laboratory, SIO Ref. 80-1, AFGL-TR-79-0257, NTIS No. ADA 085 451 (1979).

Gordon, J.I., "Implications of the Equation of Transfer Within the Visible and Infrared Spectrum", University of California, San Diego, Scripps Institution of Oceanography, Visibility Laboratory, SIO Ref. 83-10, AFGL-TR-82-0223 (1983).

Hering, W. S., "An Operational Technique for Estimating Visible Spectrum Contrast Transmittance", University of California, San Diego, Scripps Institution of Oceanography, Visibility Laboratory, SIO Ref. 82-1, AFGL-TR-81-0198 (1981a).

Hering, W.S., "Assessment of Operational Techniques for Estimating Visible Spectrum Contrast Transmittance", *SPIE Proceedings on Atmospheric Effects on System Performance,* **205**, 119-125 (1981b).

Johnson, R.W., W. S. Hering, J.I. Gordon, B. W. Fitch, and J.S. Shields, "Preliminary Analysis & Modelling Based Upon Project OPAQUE Profile and Surface Data", University of California, San Diego, Scripps Institution of Oceanography, Visibility Laboratory, SIO Ref. 80-5, AFGL-TR-79-0285, NTIS ADB 052 172L (1979).

Johnson, R.W. and B.W. Fitch, "A Review of Measured Atmospheric Optical Properties and Their Contemporary Aerosol Size Distributions", University of California, San Diego, Scripps Institution of Oceanography, Visibility Laboratory, SIO Ref. 82-22, AFGL-TR-82-0049 (1981).

Johnson, R.W., and J.I. Gordon, "Airborne Measurements of Atmospheric Volume Scattering Coefficients in Northern Europe, Winter 1978", University of California, San Diego, Scripps Institution of Oceanography, Visibility Laboratory, SIO Ref. 79-25, AFGL-TR-79-0159, NTIS No. ADA 082 044 (1979).

Johnson, R.W. and J.I. Gordon, "Airborne Measurements of Atmospheric Volume Scattering Coefficients in Northern Europe, Summer 1978", University of California, San Diego, Scripps Institution of Oceanography, Visibility Laboratory, SIO Ref. 80-20, AFGL-TR-80-0207, NTIS No. ADA 097 134 (1980).

Johnson, R.W. and J.I. Gordon, "A Review of Optical Data Analysis Related to the Modelling of Visible and Optical Infrared Atmospheric Properties", University of California, San Diego, Scripps Institution of Oceanography, Visibility Laboratory, SIO Ref. 83-5, AFGL-TR-82-0086 (1981).

Johnson, R.W. and W.S. Hering, "Measurements of Optical Atmospheric Quantities in Europe and Their Application to Modelling Visible Spectrum Contrast Transmittance", *AGARD Proceedings on Special Topics in Optical Propagation,* AGARD-CP-300, pp. 14-1 to 14-12 (1981a).

Johnson, R.W. and W. S. Hering, "An Analysis of Natural Variations in Measured European Sky and Terrain Radiances", University of California, San Diego, Scripps Institution of Oceanography, Visibility Laboratory, SIO Ref. 82-6, AFGL-TR-81-0317 (1981b).

Johnson, R.W., "Airborne Measurements of European Atmospheric Scattering Coefficients", *SPIE Proceedings on Atmospheric Effects on Radiative Transfer*, **195**, 31-38 (1979).

Johnson, R.W., "Winter and Summer Measurements of European Very Low Altitude Volume Scattering Coefficients," University of California, San Diego, Scripps Institution of Oceanography, SIO Ref. 81-26, AFGL-TR-81-0154, NTIS No. ADA 106 363 (1981a).

Johnson, R.W., "Spring and Fall Measurements of European Very Low Altitude Volume Scattering Coefficients", University of California, San Diego, Scripps Institution of Oceanography, Visibility Laboratory, SIO Ref. 81-33, AFGL-TR-81-0237, NTIS No. ADA 108 879 (1981b).

Johnson, R.W., "Daytime Visibility and Nephelometer Measurements Related to its Determination", Atmospheric Environment, **15**, 10/11, 1835 (1981c).

Johnson, R.W., "Airborne Measurements of European Sky and Terrain Radiances", University of California, San Diego, Scripps Institution of Oceanography, Visibility Laboratory, SIO Ref. 82-2, AFGL-TR-81-0275 (1981d).

Johnson, R.W., "An Experimental Device for Real Time Determination of Slant Path Atmospheric Contrast Transmittance", University of California, San Diego, Scripps Institution of Oceanography, Visibility Laboratory, SIO Ref. 82-27, AFGL-TR-82-0125 (1982).

Johnson, R.W., "An Experimental Device for Real Time Determination of Slant Path Atmospheric Contrast Transmittance (Prototype Status)", University of California, San Diego, Scripps Institution of Oceanography, Visibility Laboratory, SIO Ref. 83-14, AFGL-TR-83-0053 (1983).

Shields, J.E., "An Analysis of Infrared and Visible Atmospheric Extinction Coefficient Measurements in Europe", University of California, San Diego, Scripps Institution of Oceanography, Visibility Laboratory, SIO Ref. 82-4, AFGL-TR-81-0251 (1981).

Shields, J.E., "An Analysis of Infrared and Visible Atmospheric Extinction Coefficients Measured at One-Minute Intervals", University of California, San Diego, Scripps Institution of Oceanography, Visibility Laboratory, SIO Ref. 84-1, AFGL-TR-83-0210 (1983).

Notes